Title
Nanoscale Studies of Spin Dynamics in Confined Geometries Using Soft X-ray Transmission Microscopy

Author
Mesler, Brooke Lu

Publication Date
2010

Peer reviewed|Thesis/dissertation

Nanoscale Studies of Spin Dynamics in Confined Geometries Using Soft X-ray Transmission Microscopy

By

Brooke Lu Mesler

A dissertation submitted in partial satisfaction of the

requirements for the degree of

Doctor of Philosophy

in

Engineering Science - Applied Science and Technology

and the Designated Emphasis

in

Nanoscale Science and Engineering

in the

Graduate Division

of the

University of California, Berkeley

Committee in charge:

Professor David Attwood, Chair
Professor Yuri Suzuki
Professor Frances Hellman
Doctor Peter Fischer

Fall 2010

Abstract

Nanoscale Studies of Spin Dynamics in Confined Geometries
Using Soft X-ray Transmission Microscopy

by

Brooke Lu Mesler

Doctor of Philosophy in Engineering Science-Applied Science and Technology

University of California, Berkeley

Professor David Attwood, Chair

Understanding and controlling the manipulation of spin structures on a nanometer length scale is of primary importance to contemporary scientific investigations and future technological applications of magnetic materials. Soft x-ray transmission microscopy offers imaging with a spatial resolution down to 10 nm, and a temporal resolution of about 70 psec, with element specific magnetic contrast. As such, it is an ideal method for studying fast nanoscale spin dynamics. The focus of this dissertation is on imaging the response of magnetic vortex cores to external applied fields using soft x-ray transmission microscopy.

A technique for pinpointing vortex dynamics without time resolution was used to survey the response of a vortex core to RF fields of varying frequency and amplitude. This investigation revealed an unexpected nonlinear response of the vortex core at higher amplitude driving frequencies. Time-resolved images of the vortex core response in the linear regime were taken using a technique which phase-locked the RF driving field to the x-ray imaging pulses. These experimental images probing the frequency response of the vortex core motion are the initial step towards a deeper understanding of the behavior of the vortex core when driven by magnetic fields with frequencies near its resonant frequency.

In addition to investigating the dynamic response of a single vortex core, a magnetic system with two interacting vortex cores was studied. A patterned rectangular magnetic sample with a 7-domain magnetization configuration and two vortex cores at remanence was used in this experiment. The magnetization of this sample was imaged after the application of a fast magnetic field pulse using a pump-probe time-resolved imaging technique. The images taken showed a distortion of the vortex cores after the pulse was applied, and combined with simulation, these results provide strong evidence for the creation and annihilation of vortex-antivortex core pairs during the excitation of the initial vortices. This lends support to the many theories suggesting that a vortex-antivortex core pair is created and annihilated during the switching of vortex core polarity.

The studies outlined in this dissertation demonstrate the strength of transmission soft x-ray microscopy as a tool for investigating spin dynamics.

Contents

Acknowledgments

There are many people who have helped me through graduate school and have made this dissertation possible. First, I would like to thank my advisor, David Attwood, for his patience and support throughout my graduate career. It was a privilege to work in his group among the brightest scientists and most talented engineers I have ever encountered.

Many thanks are due to my scientific advisor Peter Fischer. As my mentor in spin dynamics studies, Peter kept me well informed of the current key issues and questions in our field of research and always pointed the way forward to future challenges. Peter is always exciting to work with, showing a boundless enthusiasm about all things magnetic.

For helpful discussions about magnetic dynamics research and magnetism in general, I must again thank Peter as well as Dong-Hyun Kim, Mi-Young Im, Julian Threatt, Kristen Buchanan, Sam Bader, and Sang-Koog Kim. The scientific collaborations I have had with Dong-Hyun, Mi-Young, and Kristen have made this dissertation what it is today.

Maintaining the soft x-ray microscope, XM-1, in prime condition is no easy task, and my experiments there would not have been possible without Peter's expert hand keeping XM-1 running smoothly. Also of great help in running experiments were Dong-Hyun, Mi-Young, Ki-Suk Lee, and Yongtao Cui. For my initial training on XM-1, thanks go out to Anne Sakdinawat and Weilun Chao. Lastly, XM-1 would not be a world class microscope without the engineers of the Center for X-ray Optics (CXRO).

The samples used in this dissertation were fabricated at the CXRO nanofabrication facility. As I worked in the nanofabrication lab, I gained invaluable knowledge from the engineers and scientists working alongside me. Specifically, for early help learning about nanofabrication and my way around the lab, I must thank Bruce Harteneck, Gerard Schmidt, Anne, Weilun, and Alex Liddle. Later in my graduate career, Erik Anderson's help mapping my sample designs onto waveguides was key to the success of my samples.

I was privileged to be a part of the student group at CXRO, the members of which taught me much about x-rays, fabrication, magnetism, and scientific research in general. I would particularly like to thank Anne, whose (slightly crazy) pranks kept everyone on their toes and laughing. Throughout my graduate career, Anne has been a mentor in many aspects of my research. Anne's support was invaluable during my last year as a graduate student; her encouragement kept me going through the end. I would also like to thank my office mate of many years, Andrew Aquila. Whether I was dodging the pieces of bookshelf he liked to swing around the office, or watching him attempt to convert everyone in the world to a tea addict, it was always entertaining and fun. As mentioned above, I am also thankful to have had many useful discussions about magnetism with Julian. To Brittany McClinton, I am grateful for an illuminating discussion about error propagation.

And lastly, I want to thank my family for their support, especially my husband Eugene Lai and our squadron of elite fighter pigs. Eugene's unwavering cheer and humor helped me endure the trials of graduate school, and my successes would not have been without his support and encouragement.

Chapter 1 Introduction

1.1 Introduction to Magnetism

From the first compass, used in ancient China for navigation as early as the 3rd century B.C., to modern magnetic storage media, which allows us to document almost every moment of our lives, magnetic materials have enabled much of human technology. While magnetic devices are abundant, there are still many questions about the fundamental properties of magnetic materials. The study of magnetism covers a diverse range of topics, from novel magnetic materials[1-3], to the response of ferromagnetic materials in a magnetic field[4-7], to current driven magnetization dynamics[8-9]. Central to each of these is the coupling of the intrinsic spin of the electron, which forms the basis of magnetic behavior. Understanding and achieving the manipulation of spin is of primary importance to contemporary scientific investigations and future technological applications.*

The simplest manipulation of spin involves the application of a magnetic field. In a sufficiently strong magnetic field, any material with a net spin per atom will become magnetized along the direction of the field (Figure 1.1(a)). For a magnetization, $\vec{M}$, defined as the total magnetic moment (spin and orbital moment) per volume, this can be expressed in terms of the external field, or Zeeman, energy[11]:

$$E_{ext} = -M_s \int \overrightarrow{H_{ext}} \cdot \vec{m}\, dV \tag{1.1}$$

Where $\overrightarrow{H_{ext}}$ is the applied external field, M_s is the saturation magnetization of the magnetic material, and $\vec{m} = \frac{\vec{M}}{M_s}$ is the reduced magnetization of the material. Typical values of M_s are on

* The manipulation of spins on the nanoscale at fast speeds is a key goal for future magnetic electronics, or spintronics. The field of spintronics has lead to historically important technologies such as read heads in hard disks, which are based on the giant magnetoresistance effect (for which Albert Fert and Peter Gruenberg were awarded the Nobel Prize in Physics in 2007). Furthermore, spintronics may lead to future applications such as the race track memory based on domain wall motion by spin polarized currents[10].

the order of several tesla[12]. From equation 1.1 we see that the energy is minimized when the reduced magnetization is parallel to the external field.

In this section introducing magnetism, other significant energies in magnetic materials are discussed as they pertain to the formation of magnetic domains and magnetic vortices. In addition, an overview of spin dynamics and the relevant timescales in magnetism is given.

1.1.1 Magnetic Domains

The spins in ferromagnetic materials will spontaneously order themselves into regions of uniform magnetization, magnetic domains. This alignment of spins without the influence of an external field is largely due to the exchange interaction (Fig 1.1(b)). The exchange interaction on the atomic level arises as a result of the Pauli exclusion principle and the Coulomb interaction[13]. Macroscopically, we can write the exchange energy as[11]:

$$E_{ex} = A \int (\nabla \vec{m})^2 \, \mathrm{dV} \tag{1.2}$$

where A is the exchange stiffness constant and can be positive or negative. Typical values of A range from 10^{-12} to $2\text{x}10^{-11}$ J/m [11]. For materials with positive values of A, spins align parallel to one another so that $(\nabla \vec{m})^2$ is reduced, thus reducing the energy of the system. Conversely, in materials with negative values of A, spins spontaneously order such that neighboring spins are antiparallel, thus increasing $(\nabla \vec{m})^2$and reducing the energy of the system. Materials with positive values of A are ferromagnets and those with negative values of A are antiferromagnets. The experiments outlined in this dissertation used Permalloy ($Fe_{20}Ni_{80}$), a ferromagnetic material.

Rather than having completely uniform magnetization due to the exchange interaction, magnetic samples usually have magnetic domains because several competing energies dictate the arrangement of spins. Aside from the exchange energy, another significant energy in this balance is the magnetostatic, or stray field, energy which can be written as[11]:

$$E_s = \frac{\mu_0}{2} \int (\mathrm{H_d})^2 \, \mathrm{dV} \tag{1.3}$$

where $\mu_0 = 4\pi \, x \, 10^{-7} \frac{Wb}{A \, m}$ is the vacuum permeability, and $\overrightarrow{\mathrm{H_d}} = \mathrm{N_d}\vec{M}$ is the demagnetizing field. $\mathrm{N_d}$ is dependent solely on the shape of the magnetic sample[14]. As can be seen in Figure 1.1(c), $\overrightarrow{\mathrm{H_d}}$ is a field that is oriented opposite to the magnetization of a ferromagnet. Another way to conceptualize this energy is in terms of the stray field†. Arranging the magnetization so as to minimize the field generated outside of the material will minimize the magnetostatic energy.

† Stray fields exist because the magnetic induction, $\vec{B} = \mu_0 \vec{H} + \vec{M}$, must form a closed loop. This means a configuration of $\vec{M}$ with poles, like that in Figure 1.1(c), must result in a stray magnetic field, $\vec{H}_s$. The stray field, $\vec{H}_s$, and demagnetizing field, $\vec{H}_d$, are oriented in opposite directions such that the total magnetic field along a closed loop sums to zero.

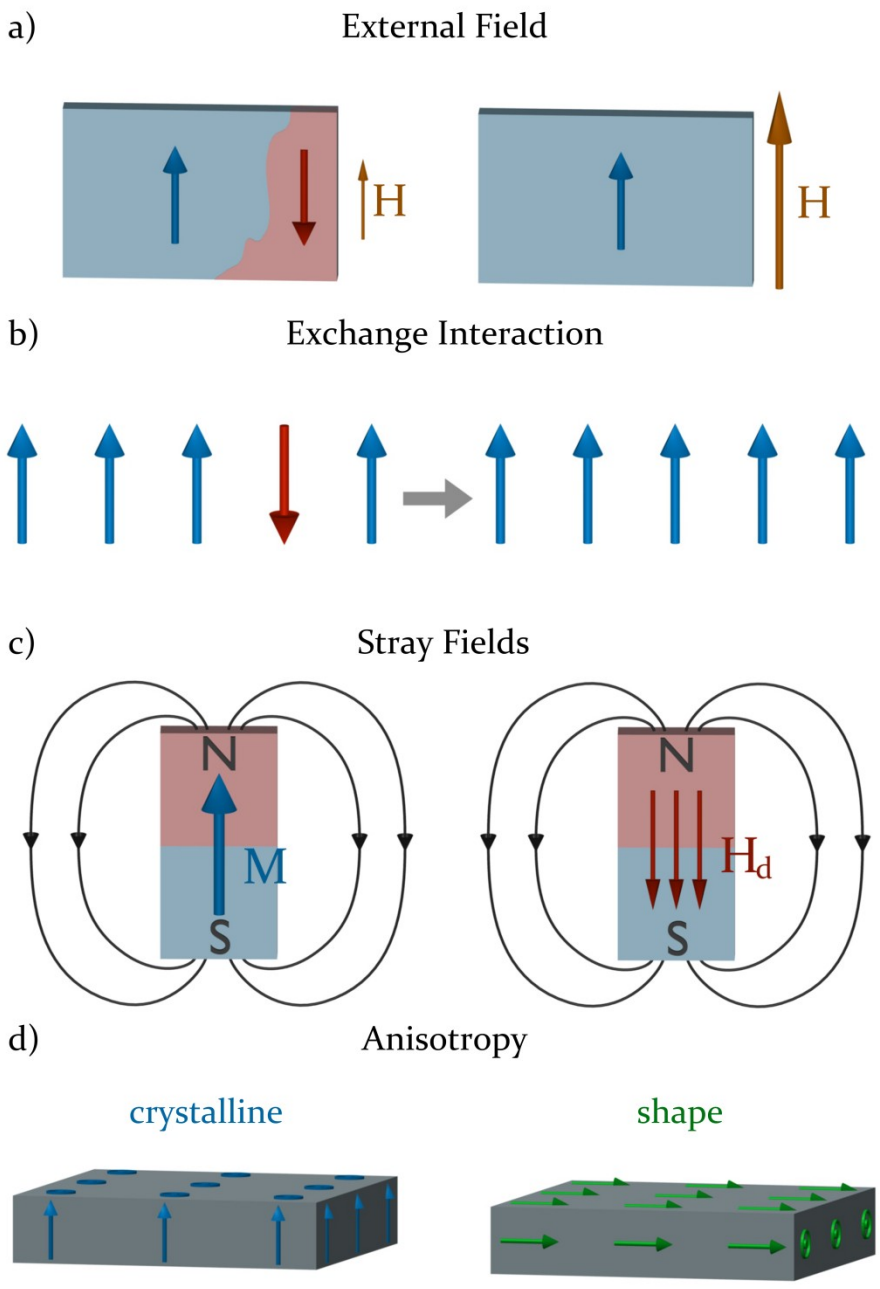

Figure 1.1 Important energies for magnetic systems. a) Magnetization tends to align with an external field. A magnetic material will become uniformly magnetized under a strong enough external field. b) The exchange interaction causes ferromagnetic materials to have ordered spins. c) A large stray field from a magnet leads to a significant demagnetizing field, $\overrightarrow{H_d}$, and thus a larger magnetostatic energy term. d) Anisotropies cause a preference for magnetization in certain directions. A strong enough crystalline anisotropy can cause magnetization perpendicular to the plane of a thin magnet, contrary to the shape anisotropy which leads to a preference for in-plane magnetization to minimize the magnetostatic energy.

Comparing just the exchange and magnetostatic energies, the origin of magnetic domains becomes clear. Figure 1.2 shows a progression of magnetization configurations from an exchange dominated configuration in (a) to a balanced configuration in (c). The domain configuration in Figure 1.2(c) is called a flux closure state or vortex state. Domains allow the magnetization to be arranged so that stray fields are eliminated, or minimized, and also allow the alignment of spins over large areas. The transitions between domains, i.e. domain walls, will be addressed briefly later.

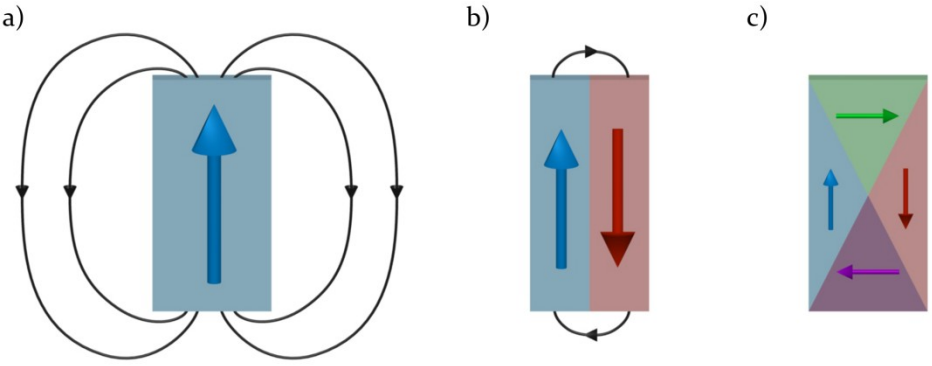

Figure 1.2 Exchange energy vs. magnetostatic energy. a) The magnetostatic energy is large while the exchange energy is minimized. b) The magnetostatic energy is reduced and the exchange energy is increased slightly due to the antiparallel magnetizations along the middle of the structure. c) The magnetostatic energy is minimized. While the exchange energy is again large where the magnetization changes between domains, recall that the domains in b) and c) still lower the exchange energy as they are large regions of uniform magnetization.

The arrangement of domains in a magnetic material can also be significantly affected by anisotropies of the sample (Fig 1.1(d)). A strong anisotropy can result in easy axes or easy planes where the strength of the magnetic field needed to magnetize along that direction, or in that plane, is much less than for other directions or planes in the material. The magnetostatic energy discussed above can be seen as shape anisotropy. In Figure 1.2(a) the magnetization is shown pointing initially along the long axis of the rectangle because this results in less stray fields than other uniformly magnetized configurations such as perpendicular to the long axis or normal to the plane of the sample. Another anisotropy commonly encountered is magnetocrystalline anisotropy. Magnetocrystalline anisotropy results from coupling between the crystalline lattice of a material and the spins on the lattice; this is achieved through spin-orbit coupling[13]. The energy contribution from magnetocrystalline anisotropy for a magnetic material with uniaxial anisotropy can be written as[11]:

$$E_{ani} = \int (K_1 \sin^2\theta + K_2 \sin^4\theta + \cdots) dV \qquad (1.4)$$

where θ is the angle between the magnetization and the easy axis and the K_n are constants where usually K_1 is much larger than the successive K_n. Typical values of the K_n range from 10^2 to $2\text{x}10^7$ J/m^3 [11].

The studies outlined in this dissertation use patterned $Fe_{20}Ni_{80}$ samples with areal dimensions on the order of a micron and thicknesses of 100 nm and less. With a face-centered cubic crystalline structure, $Fe_{20}Ni_{80}$ would be expected to have cubic magnetocrystalline anisotropy. However, evaporated films of $Fe_{20}Ni_{80}$ have a very slight induced uniaxial

anisotropy[15], where the constant K_1= 5 x10^2 J/m^3[10]. This small magnetocrystalline anisotropy of $Fe_{20}Ni_{80}$ means that the shape anisotropy resulting from the geometrical confinement is the most significant anisotropy for these samples. As an easily magnetized, soft, ferromagnet with minimal anisotropies, $Fe_{20}Ni_{80}$ is an ideal material for studies of patterned magnetic elements.

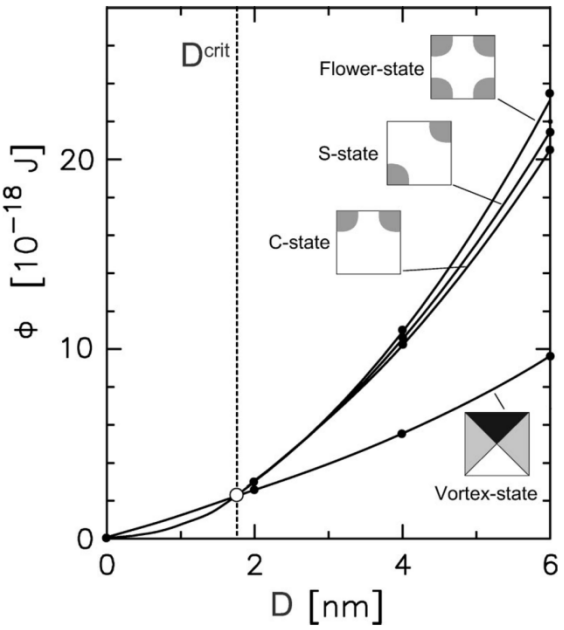

Figure 1.3 Phase diagram of domain configurations for thin 1μm x 1μm $Fe_{20}Ni_{80}$ squares. Here φ is the calculated total energy and D is the thickness. The Flower-state, S-state, and C-state are quasihomogenous single domain states where the shaded regions depict areas where the magnetization curves slightly. From this graph it is clear that the vortex state is preferable above about 2 nm thickness. Figure from [12].

Patterned elements with dimensions on the order of a micron have well known remanent states with either uniform magnetization or a vortex magnetization (Fig 1.3). There are two characteristic lengths, both often called the exchange length, that can help predict which type of magnetization will lower the energy the most. We can define $\Delta = \sqrt{A/K}$ and $\Delta_d = \sqrt{A/K_d}$ where A is the exchange stiffness constant, K is an anisotropy constant, and K_d is the stray field constant [11]. If an element is comparable in size to the length Δ and larger than Δ_d, then a simple multidomain structure such as a vortex will form. If, however, it is smaller than Δ_d it will be a single domain element. For $Fe_{20}Ni_{80}$, Δ=161.2 nm and Δ_d=5.7 nm [12].

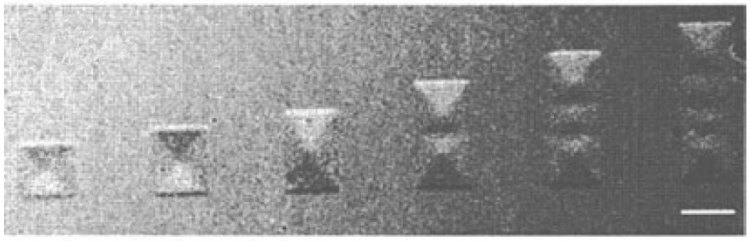

Figure 1.4 Rectangular $Fe_{20}Ni_{80}$ elements with thicknesses of 50 nm and aspect ratios of: 1:1, 1:1.3, 1.1.5, 1:2, 1:2.5, and 1:3. Up to an aspect ratio of 1:3, a 4-domain Landau pattern occurs, for larger aspect ratios a more complex domain structure evolves. Scale bar is 1 μm. Images were taken at the Ni L_3 edge using soft x-ray transmission microscopy. Figure from [16].

Patterned $Fe_{20}Ni_{80}$ elements often have domain structures forming one or more closed loops of magnetization depending on the geometry of the structure (Fig. 1.4). Figure 1.5 depicts a 7-domain Landau pattern commonly seen in thin $Fe_{20}Ni_{80}$ rectangles with areal dimensions on the order of a few microns and thicknesses of tens of nanometers. A study of the spin dynamics in a sample exhibiting this domain configuration is covered in Chapter 4.

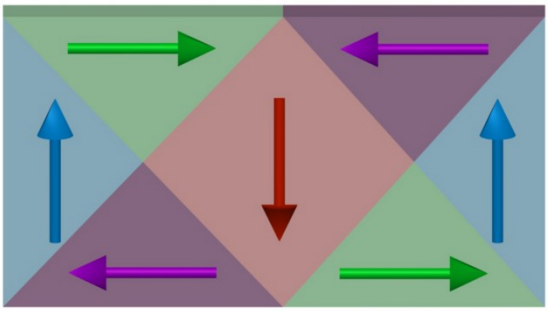

Figure 1.5 7-domain Landau pattern.

Transitions between domains are called domain walls, where the magnetization continuously changes to transition between the different directions. In bulk magnetic materials Bloch walls form; in these walls the magnetization rotates gradually parallel to the plane of the wall, eliminating poles within the wall. These walls have a thickness on the order of the material's anisotropy exchange length, Δ. Anisotropy is the key parameter here as the rotation of the magnetization will align it off the easy axis along which the domains are magnetized[11]. In thin films, where the thickness of the film becomes comparable to the wall width, Bloch walls are generally not energetically favourable and Néel walls form. Néel walls rotate in the plane of the material, eliminating stray fields. In these walls the width is on the order of the stray field exchange length, Δ_d, or the film thickness[11].

In small structures with no sharp corners, e.g. thin cylinders with thicknesses of tens of nanometers and radii on the order of a micron, a vortex structure can form with no domain walls, only a gradual change in magnetization as can be seen in Figure 1.6 [17-19]. In such geometries the magnetization can be ordered always tangent to the sides of the material to eliminate stray fields. As with the square patterns analyzed in Figure 1.3, small rounded structures are uniformly magnetized and once the pattern is large enough that the magnetostatic energy is

significant, a vortex state forms. The central region of the vortex structure shown in Figure 1.6, where the magnetization points out of the plane, will be discussed further in the next section.

Figure 1.6 Magnetic vortex structure.

1.1.2 Magnetic Vortices

In Figure 1.6 the magnetization lies in the plane over most of the sample area; however, in the center, the magnetization begins to twist out of the plane until finally at the very center there is an area of magnetization normal to the plane of the sample. This region of out-of-plane magnetization is called the vortex core. Vortex cores form in the center of vortex states, both in rounded elements without domain walls and in squared patterns with domains. The 7-domain Landau pattern shown in Figure 1.5 has two vortex cores, one at the center of each flux closure loop.

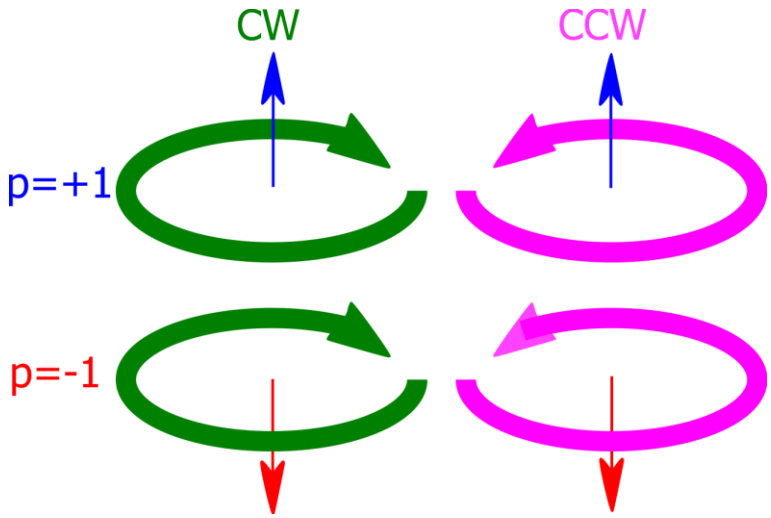

Figure 1.7 The four configurations of a vortex state. The green and pink circular arrows indicate clockwise and counter-clockwise in-plane magnetization, respectively. The blue and red arrows indicate the vortex core polarization up out-of-the plane and down into the plane, respectively.

Vortex states like that shown in Figure 1.6 can have four possible configurations: two potential in-plane configurations, a clockwise and counterclockwise flux closure loop, and two potential polarities (Fig. 1.7). The polarity of a vortex state is defined by the direction of magnetization of the core with values of p=±1. The core polarity is a significant parameter as it can dictate the dynamic response of the vortex. The polarity of the core dictates the sense of rotation of the vortex core during gyrotropic motion, where the core moves in a circular path around its original location. Regardless of the in-plane magnetization, a vortex core with p=+1 will rotate counterclockwise and a vortex core with p=-1 will rotate clockwise[5]. The experiment described in Chapter 4 shows another example of the vortex core polarity dictating the dynamic response of the magnetic configuration.

The size of vortex cores, like the size of domain walls, is dictated by competing energy terms. The magnetostatic energy is clearly increased with larger vortex cores which create stray fields. However, the formation of the vortex core reduces the exchange energy as the magnetization on either side of the core, which is antiparallel, gradually is rotated until the magnetization at the center is parallel; with no vortex core the magnetizations at the center would be rapidly changing. The size of the vortex core is on the order of the stray field exchange constant, Δ_d [11].

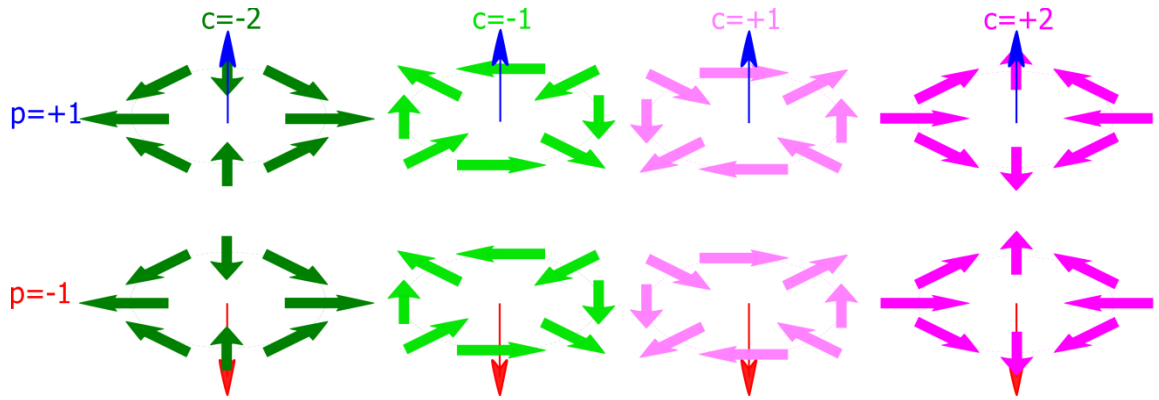

Figure 1.8 Configurations of antivortex core states. Here $\boldsymbol{c = 2\varphi_0/\pi}$, where $\boldsymbol{\varphi_0}$measures the angle between the horizontal axis and the magnetization of the right most magnetization.

There is another magnetic structure with an out-of-plane core called an antivortex. Like the vortex core, the antivortex core can have two polarities, but rather than turning around the core, the in-plane magnetization turns out away from the core (Fig. 1.8). All in-plane configurations of the antivortex are identical after rotation, but a parameter c can be defined such that $c = 2\varphi_0/\pi$, where φ_0 is the angle of the magnetization with respect to a chosen axis[20]. Such a definition allows the orientation of the antivortex to be defined with values of c ranging from -2 to +2.

Antivortices can be isolated, such as in patterned shapes with interlocking ring geometries where the curve of the rings matches the natural curve of the antivortex magnetization (Fig. 1.9(a)) [20-21], and also are commonly seen paired with vortices, such as in cross-tie walls, domain walls formed by a chain of vortex and antivortex cores (Fig. 1.9(b)) [21-23].

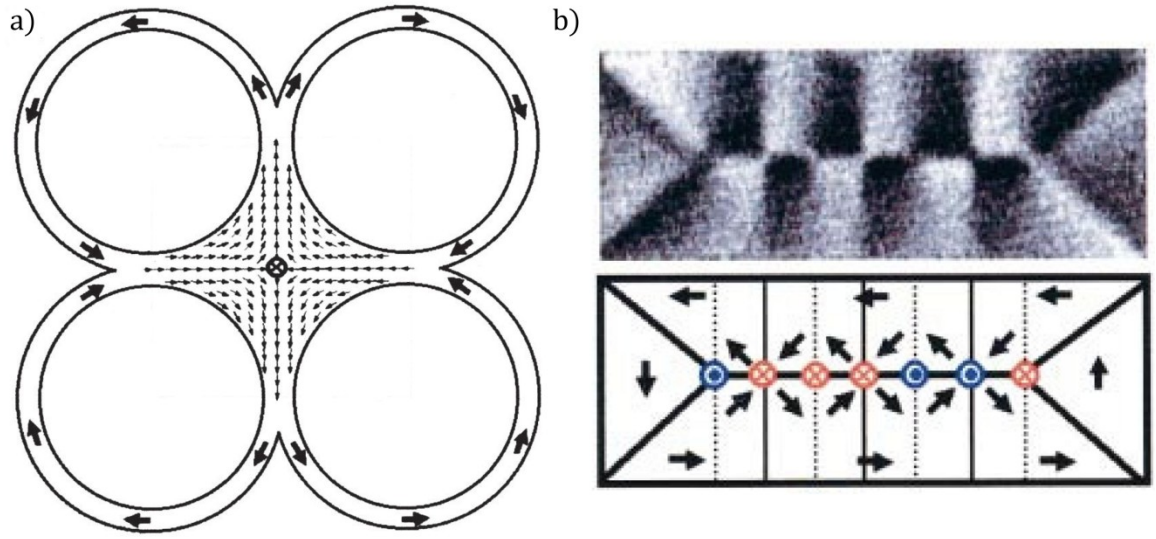

Figure 1.9 Antivortices. a) Schematic of an isolated antivortex. b) Experimental magnetic force microscopy image of a cross-tie wall with corresponding schematic below. Blue indicates magnetization up out of the plane and red indicates magnetization down into the plane. Figures from [21].

The two polarities of magnetic cores make them ideal candidates for information storage technologies[24-25]. In addition to the binary nature of the vortex core polarity, the vortex state is extremely stable, requiring an applied field of about 2 kOe to switch the polarity of a vortex core in a $Fe_{20}Ni_{80}$ cylinder with a 1μm diameter and an 80 nm thickness[25]. Current research is exploring efficient methods of switching the vortex core[26-28]. It has been revealed that by first exciting a lateral motion of the vortex core, the switching of the core polarity is facilitated. It has been demonstrated that the core polarity can be switched with both electric currents and magnetic fields[4,26]. In this dissertation the behavior of excited vortices is examined with both oscillating fields (Chapter 3) and field pulses (Chapter 4). Studies such as these provide a more detailed understanding of the dynamic response of the vortex which could enable the development of writing techniques for information storage technology utilizing vortex states.

The information storage potential of vortex cores extends even beyond a control of the core polarity. Investigations have been done through micromagnetic simulations which suggest that the position of a vortex core in a patterned structure could be used to store more information. With nine distinct positions of a vortex core in a specially designed disk with needle-like protrusions, and taking into account the 4 states of a vortex core, a single pattern could exhibit 36 different states[29].

1.1.3 Spin Dynamics

There are many fascinating areas of spin dynamics with different driving or exciting mechanisms and different time scales of interest. To roughly examine which phenomena occur at what time scale, the Heisenberg uncertainty principle can be employed: $\Delta E \Delta t \sim \hbar$, where E is energy, t is time and $\hbar$ is Plank's constant divided by 2π. Thus, dynamics corresponding to the strongest interaction, exchange, are described on a femtosecond timescale, while reactions due to magnetic anisotropies need only a subnanosecond time resolution[13].

The manipulation of spins with applied fields is central to contemporary technology, and there are still many dynamic behaviors in this field that have yet to be fully understood and investigated. One question of great technological, as well as fundamental, interest is how fast one can flip a magnetization.[‡] When an external magnetic field is applied to a ferromagnetic material, it can take several nanoseconds to switch the magnetization due to the magnetization precessing around the field and gradually damping down to align with the applied field[32]. Special engineering of the applied field pulse can stop the precession and achieve switching after about 200 ps, 10 times faster than the ordinary damping method[33].

Ultrafast switching of magnetization has been achieved through the application of subpicosecond laser pulses. It has been demonstrated that a write-read time of 30 ps can be achieved through such a method[34]. This switching mechanism excites the material, reducing the magnetization linearly and exciting the surrounding lattice until the magnetization comes back antiparallel to its original configuration.

Magnetization can also be switched by applying spin-polarized currents to magnetic materials where the angular momentum from the current is directly transferred to the

[‡] An ultimate limit of 2 ps for deterministic precessional switching of magnetization using an applied magnetic field was described by I. Tudosa et al.[30]. Using 40 fsec circularly polarized laser pulses, C. D. Stanciu et al. were able to reproducibly switch the magnetization in GdFeCo on a subpicosecond timescale [31].

magnetization[13,35]. The application of current through a magnetic material in order to manipulate the spins in the material is receiving great attention due to possible technological applications in devices with reduced areal dimensions such as vertical race track memory where, through the application of current, magnetic domains are moved through a material as though on a track[36-38].

The experiments described in this dissertation have a time resolution of 70 ps, which allows for the examination of dynamics involving domain wall and vortex core motion in response to an external field. In the future, x-ray microscopy studies using fsec x-ray sources will allow exchange dominated dynamics to be studied; however, for the present, there are still many unanswered and important questions to be examined on the 100 ps timescale such as the trajectory of a vortex core when an oscillating magnetic field is applied.

1.2 Soft X-ray Transmission Microscopy

To further our understanding of nanoscale spin dynamics, advanced analytical tools are necessary. Soft x-rays, characterized by energies ranging from about 250 eV to several keV [39], are well suited for such studies. Soft x-ray transmission microscopy is an excellent probe for magnetic dynamics, offering high spatial and temporal resolution[40-41]. This section introduces soft x-ray transmission microscopy, beginning with a discussion of x-ray transmission. Later XM-1, a full field soft x-ray transmission microscope is described. Key features of XM-1 are further described with individual discussions of zone plates, x-ray magnetic circular dichroism (XMCD), and bending magnet radiation. The section closes with an overview of imaging magnetic materials with XM-1.

Fundamentally, soft x-ray transmission microscopy detects the transmitted intensity of photons through a material, which can be written as[39]:

$$\frac{I}{I_0} = e^{-\rho\mu x} \tag{1.5}$$

Where I is the transmitted intensity, I_0 is the initial intensity, ρ is the mass density of the material, μ is the mass absorption coefficient, and x is the thickness of the material. The parameter μ is dependent on both the elements probed and the energy of the photons; absorption of soft x-rays is substantially increased at element specific absorption edges. This element specificity arises due to the localized nature of the 2p-shell electrons which have binding energies well matched by soft x-ray radiation, and is extremely beneficial to x-ray microscopy, providing element specific images.

For spin dynamics studies, the most important phenomenon occurring during soft x-ray absorption is the XMCD effect which occurs at the L absorption edges of ferromagnetic materials[42]. Due to XMCD, the mass absorption coefficient, μ, is also dependent on the projection of the incident photon helicity onto the material magnetization. For example, at the iron (Fe) L_3 absorption edge (707 eV photon energy), right and left circularly, or elliptically, polarized x-rays transmitted through an Fe thin film with some component of the film magnetization on the axis of the photon propagation direction will have different μ for identical regions of the film. This effect provides a direct probe of the magnetic moments in a material and will be discussed further later in this chapter.

1.2.1 XM-1: A Full Field X-ray Transmission Microscope

The experiments outlined in this dissertation were run at XM-1, a full field soft x-ray transmission microscope[43]located at beamline 6.1.2 at the Advanced Light Source (ALS) in Berkeley, CA[39]. A schematic of XM-1 is shown in Figure 1.10 where the critical components of the microscope are illustrated.

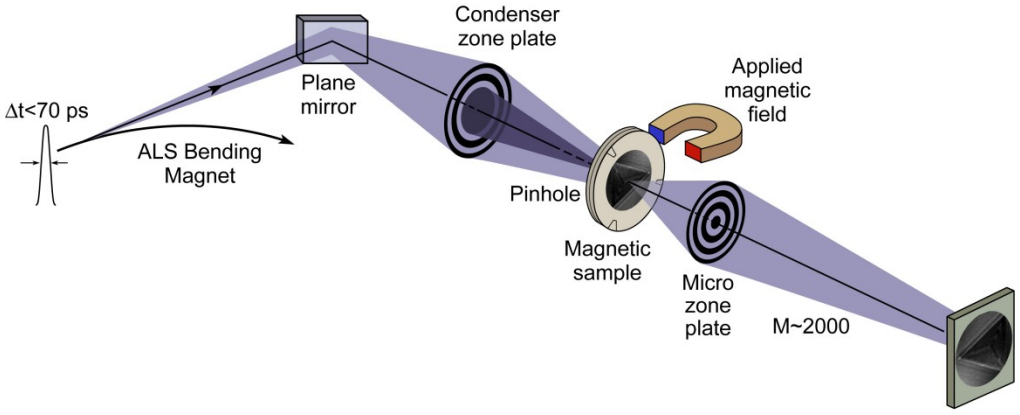

Figure 1.10 Schematic of XM-1 a full field soft x-ray transmission microscope. The magnetic sample shown is a $Fe_{20}Ni_{80}$ patterned triangle with 100 nm thickness and 2 μm edge length. M~2000 for a Micro zone plate with outer most zone width of 25 nm. Figure from [44].

XM-1 can generally be described in the same terms as a tabletop visible light microscope; there is a light source, illuminating optics, a transmissive sample, resolving optics, and a camera to record the images. The light source is soft x-rays from a bending magnet at the ALS; this type of radiation is elliptically polarized off axis as will be discussed further below. Optics for soft x-ray manipulation are quite different from the traditional lenses employed for visible light. Due to the short absorption length of soft x-rays and their small angles of refraction, nontraditional solutions have been found[39]. Fresnel zone plates are diffractive optics which can be designed to focus soft x-rays and are used both for illumination and resolving optics at XM-1. Zone plates will be discussed in more detail below.

1.2.2 Zone Plates for X-ray Microscopy

A zone plate is a circular diffraction grating consisting of alternating opaque and transmissive rings, or zones, which are scaled progressively smaller moving from the center outwards (Fig 1.11).

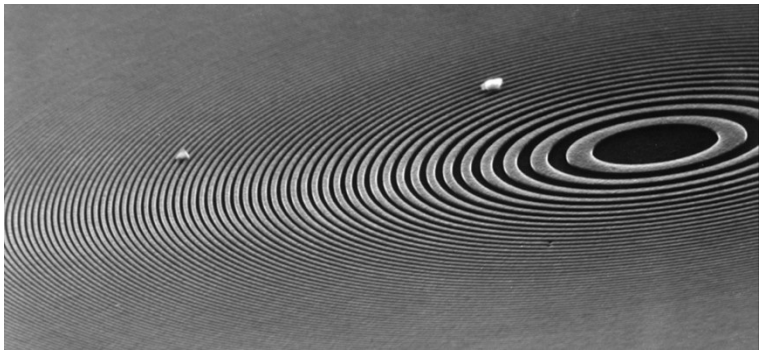

Figure 1.11 Fresnel zone plate. Figure courtesy of E. Anderson, LBNL.

The zones are designed such that light of a specific wavelength passing through the zone plate will be diffracted to a focus. The angle θ at which light is diffracted from a transmission grating can be described by[39]:

$$\sin\theta = \frac{\lambda}{d} \tag{1.6}$$

where λ is the wavelength of light, and d is the period of the grating. Examining equation 1.6 and referencing Figure 1.12, it is clear that by reducing the period of the grating as the distance from the central axis is increased, the diffraction angle can be appropriately increased, thus bending off axis light more sharply back to the axis. In order for the diffracted light to constructively interfere at the focus, the radii of the zone must be engineered appropriately. As depicted in Figure 1.12, the radius of the nth zone is designed such that the path length the light must travel to reach a horizontal distance f away from the zone plate is $f + \frac{n\lambda}{2}$. Recalling that every other zone is opaque, this arrangement of the zone radii allows for constructive interference at f, the focus, which can be described by[39]:

$$f \cong \frac{4N(\Delta r)^2}{\lambda} \tag{1.7}$$

Where N is the total number of zones and Δr is the outermost zone width. The dependence of the focal length on wavelength allows a simple monochromator design at XM-1. Referring to Figure 1.10, the condensing optics consist of a zone plate and a pinhole (not shown). The pinhole serves to select the focused light of a specific energy, or wavelength.

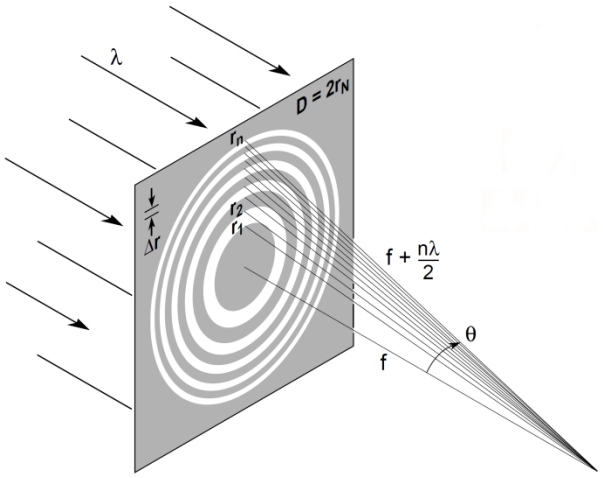

Figure 1.12 First order diffraction focus in a zone plate. Figure from [39].

The spatial resolution achievable with zone plates is approximately equal to the outermost zone width, Δr. Fabricating zone plates with increasingly smaller zones is an engineering challenge. At the present time XM-1 operates with a typical resolution of about 25 nm, and under special operation a resolution down to 10 nm has been achieved[45]. As seen in equation 1.7, a smaller Δr results in a smaller focal length. Considering a standard zone plate at XM-1 with 625 zones and an outermost zonewidth of 25 nm, a typical operating wavelength of 1.75 nm results in a focal length of less than a millimeter. The even shorter focal lengths corresponding to the highest resolution zone plates pose an engineering challenge for future magnetic studies with x-ray microscopy. To some extent longer focal lengths can be achieved by increasing N, the number of zones; however, for the zone plate to maintain its focusing properties the spectral bandwidth of the incident photons must be less than $\frac{\lambda}{N}$.

1.2.3 X-ray Magnetic Circular Dichroism

There are numerous approaches to imaging with magnetic contrast. A commonly used technique is magnetic force microscopy (MFM), where the stray fields of a magnetic material interact with a scanning tip to create an image[46]. MFM can provide very high spatial resolutions, but, due to the scanning nature of the technique, has limited potential in time-resolved studies. Another way to probe magnetization is through analyzing the rotation of the plane of polarization of an incident photon beam as it is reflected off of, or is transmitted through, a magnetic material[47]. In reflection this phenomenon is called the Kerr effect, or the magneto-optical Kerr effect (MOKE), and in transmission it is called the Faraday effect, or Faraday rotation.[§] These effects in the visible light range can provide magnetic imaging with high temporal resolution using fast visible light lasers, but are ultimately limited in spatial resolution by the wavelength of light. Images with high spatial resolution and magnetic contrast can be obtained with photon emission electron microscopy (PEEM) [48] and soft x-ray microscopies[43] both of which take advantage of XMCD. Time-resolved studies are also possible with these techniques due to the inherent time structure of x-ray sources.

[§] The XMCD effect is the x-ray counterpart of these optical effects.

Offering high spatial and temporal resolution, XMCD is perhaps the most powerful route to imaging with magnetic contrast. The XMCD effect around the Fe L_3 and L_2 edges, absorption edges corresponding to the $2p_{3/2}$, to 3d and $2p_{1/2}$ to 3d electron excitations, respectively, is shown in Figure 1.13. The difference in absorption between two opposing magnetization directions can be up to 50%. This is a large effect compared to the MOKE contrast in Kerr microscopy or other similar phenomena such as Faraday rotation with extreme ultraviolet radiation[49].

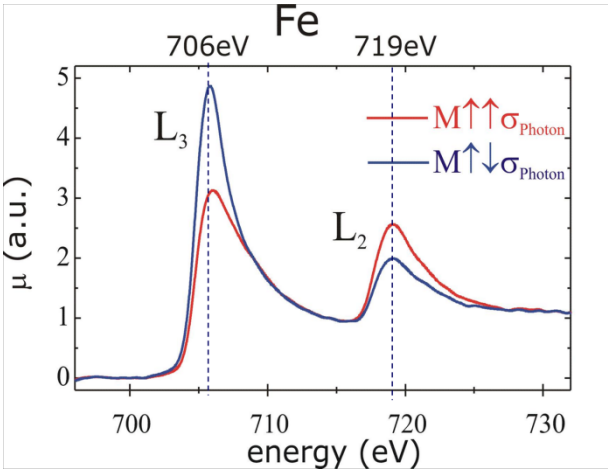

Figure 1.13 The mass absorption coefficient, $\boldsymbol{\mu}$, vs. photon energy of circularly polarized x-rays for a thin Fe film around the L_3 and L_2 edges. The red and blue lines are for the cases of parallel and antiparallel orientations of the magnetization of the photon helicity, respectively. Figure from [50].

The origin of XMCD can be explained using a two-step model of absorption[13]. In the first step, incident x-rays "polarize" an electron in the 2p shells, giving it spin and orbital momentum. In the second step, the electron is selectively absorbed by the 3d band depending on the spin and orbital "polarization" of the electron. This simply translates to the well known selection rules for electron excitation with the addition of spin, where a spin up electron in a 2p shell can only be excited to a spin up state in the 3d band by a photon with helicity equal to $+\hbar$ [13]. Essentially, this interaction probes the empty density of states in the 3d band. While the total number of spin up and spin down states in the 3d band is identical, the spin up and spin down 3d bands are shifted with respect to one another in energy due to the exchange interaction. This exchange splitting leads to a different density of states for spin up and spin down electrons at the Fermi level, resulting in a net magnetic moment. Considering that a full 3d band has no magnetic moment, one can see that the hypothetical magnetic moment of the unoccupied states, or hole moment, is the negative of the actual magnetic moment. Thus, the XMCD spectrum is a direct probe of the magnetic moment in a ferromagnetic material.

Experiments providing detailed absorption spectra can provide quantitative information about the spin and orbital moments in a magnetic material. By measuring the absorption with both right and left circularly polarized light, a difference spectrum can be calculated which shows the XMCD effect at the absorption edges. Using the sum rules, the spin moment per atom, and the average orbital moment per atom, can be calculated using the areas under the absorption peaks in the difference spectrum[13]. For studies at XM-1, XMCD provides magnetic contrast in the images, where dark and bright areas of the image indicate oppositely magnetized domains.

1.2.4 Bending Magnet Radiation

The illumination source at XM-1 is a bending magnet at the ALS. Bending magnet radiation is generated when electrons moving at relativistic speeds are accelerated by a bending magnet, a simple case of the trajectory of a charged particle moving in an arc in the presence of a magnetic field[39]. A schematic of bending magnet radiation is shown in Figure 1.14. The blue and red colors of the x-ray beam are a rough indication of the polarization of the x-rays.

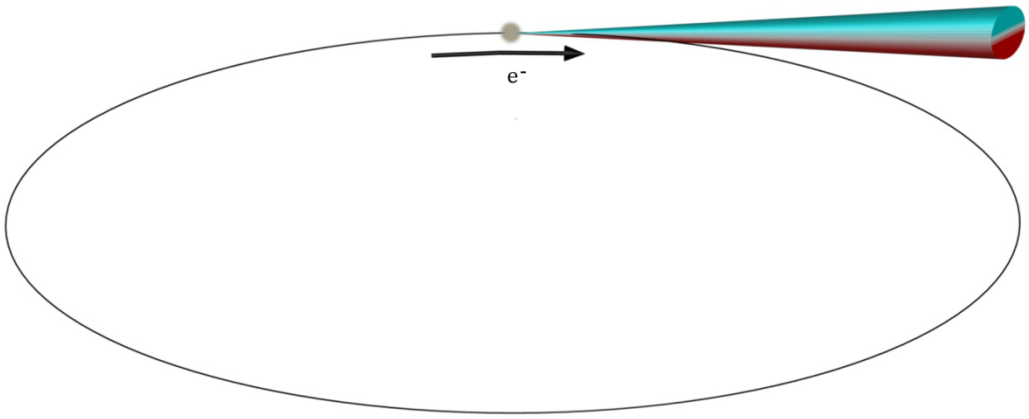

Figure 1.14 Bending magnet radiation.

Bending magnet radiation, while linearly polarized on axis, is elliptically polarized in opposite senses off axis where the polarization becomes stronger farther out of the plane of the synchrotron. This can be seen in Figure 1.15, where calculations of the horizontally polarized photon flux and vertically polarized photon flux are plotted. The phase shift between these two components leads to a net elliptical polarization.

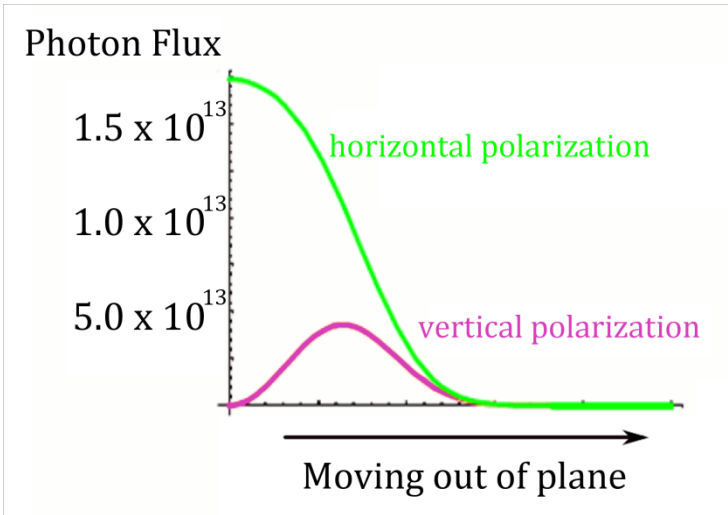

Figure 1.15 Unequal photon fluxes of horizontal and vertical polarized light lead to elliptically polarized bending magnet radiation.

At XM-1, a slit system is positioned such that only a portion of the bending magnet radiation is used to illuminate the microscope[51]. By changing the vertical position of the slit, oppositely elliptically polarized x-rays can be selected.

1.2.5 Imaging Magnetic Materials with XM-1

XM-1 provides full field imaging with high resolution element-specific magnetic contrast[43]. In-plane or out-of-plane magnetization can be imaged by altering the angle of the sample with respect to the incident photon beam. Samples are oriented perpendicular to the incident photons to image out-of-plane magnetization, and are oriented at a 60 degree angle to image in-plane magnetization. The magnetic contrast from the images can be enhanced by utilizing both right and left elliptically polarized radiation from the bending magnet (Fig 1.16). Soft x-ray transmission microscopy is an excellent method for imaging static magnetic configurations; moreover, it can be extended further to image spin dynamics[44,52-53]. Several experimental techniques used to study spin dynamics at XM-1 will be covered in Chapter 2.

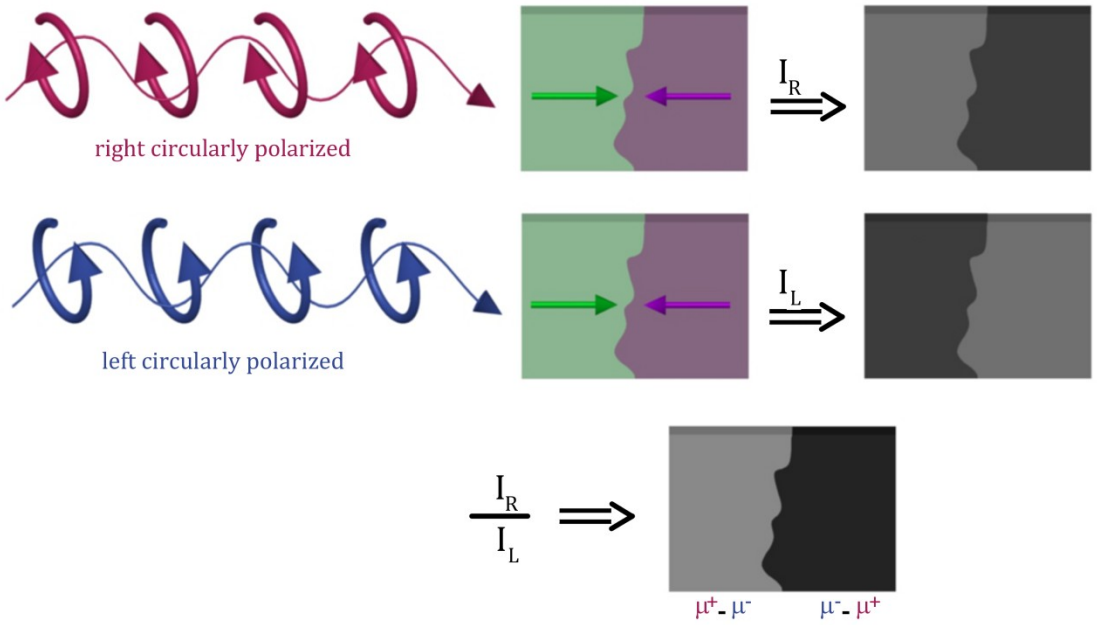

Figure 1.16 Enhanced magnetic contrast from XM-1 images. Schematic of the absorption at the Fe L_3 edge where more absorption occurs when the photon helicity is antiparallel to the magnetization. I_R and I_L are the intensities after transmission through the magnetic material for right and left circularly polarized x-rays, respectively. μ+ and μ- are mass absorption coefficients for parallel and antiparallel alignment of the magnetization and the photon helicity. (In-plane magnetized samples such as are depicted must, in reality, be situated at an angle to place a component of the magnetization along the axis of the photon helicity).

1.3 Dissertation Overview

This dissertation examines several methods for performing spin dynamics experiments using soft x-ray transmission microscopy. Specifically the dynamic response of magnetic vortex cores to external fields is studied. Vortex dynamics studies such as those described in this dissertation lead to a deeper understanding of vortex cores, which may enable novel information

storage technologies. The first magnetic images showing evidence of the nonlinear response of a vortex core to high amplitude magnetic fields are presented in this dissertation. In addition, a first attempt to make a detailed experimental study of vortex core trajectories when driven by RF fields with a variety of frequencies around the resonant frequency is described. These two studies aim for a more complete understanding of the resonant gyrotropic motion of a vortex core, which will be significant in understanding how a "bit" of information in a magnetic vortex core storage device will be written. Finally, a study of the magnetization dynamics in a thin rectangular magnetic sample provides some of the only clear experimental evidence of vortex-antivortex pair creation and annihilation during the excitation of a vortex core. This study provides insight into the spin dynamics that take place as a vortex core polarity is switched, which again expands on our understanding of how information in a magnetic vortex core storage device will be written

In Chapter 2 the experimental and fabrication techniques used in these studies are described. Specially designed samples fabricated on transmissive substrates facilitate the application of magnetic fields to the magnetic patterned elements. Three different experimental techniques are described: dynamics studies using non time-resolved imaging, and time-resolved imaging methods employing phase locking and pump probe techniques.

In Chapter 3 resonant vortex core dynamics are examined in thin $Fe_{20}Ni_{80}$ disks. In a broad survey of the dynamic vortex core response to oscillating fields of varying frequency and amplitude, an unexpected nonlinear response is seen for high amplitude RF fields. The vortex core motion in the linear regime is examined further using a phase locking technique. Preliminary work on imaging the trajectory of the vortex core when excited by frequencies near resonance is detailed.

In Chapter 4 a study of a thin rectangular $Fe_{20}Ni_{80}$ sample is covered. The magnetization of this sample is perturbed with a short field pulse, and the dynamic response includes the generation of vortex-antivortex core pairs.

Chapter 2 Spin Dynamics Studies at XM-1: Sample Fabrication and Experimental Technique

Spin dynamics experiments require specialized sample fabrication and experimental technique. The first sections in this chapter describe the key processes used to fabricate samples for spin dynamics. UV contact lithography is used to define waveguides as well as membranes, which together form the sample substrate. E-beam lithography is used to fabricate the patterned magnetic samples themselves. The final sections in this chapter detail three experimental techniques for spin dynamics studies: time-averaged imaging, time-resolved imaging using a phase-locking technique, and time-resolved imaging using a pump-probe technique.

The studies described in this dissertation use external magnetic fields to perturb the magnetization in the samples. In order to apply fields in a controlled manner, the magnetic samples were designed to sit on waveguides through which current pulses could be applied to create Oersted field pulses at the sample. Figure 2.1 depicts the full sample and holder on several different length scales, emphasizing the design of the waveguide as its areal dimensions are gradually reduced down to the 10 μm wire where the magnetic samples rest. As these experiments focused on spin dynamics in confined geometries, the $Fe_{20}Ni_{80}$ samples were patterned into shapes with areal dimensions on the order of a micron using e-beam lithography. Finally, because the experiments used soft x-ray transmission microscopy the substrates used needed to be transmissive. Silicon nitride (Si_3N_4) was used as the substrate in these experiments as it is an ideal material for fabricating thin transmissive membranes, as will be discussed later in this chapter. The specific substrate and sample design described in this dissertation required the fabrication of the waveguides first, followed by the fabrication of the Si_3N_4 membranes, and lastly the fabrication of the patterned $Fe_{20}Ni_{80}$ samples.

Three distinct techniques for obtaining information about spin dynamics are described in this dissertation. First, a useful method of investigating the dynamic spin response without time resolution is outlined. Next, two time-resolved techniques are described. The first is a phase-

locking technique where a continuous RF field is applied to the sample in phase with the probing x-rays, and the second is a pump-probe technique where a fast field pulse is applied to the sample and which is then probed with x-rays as the spins respond to the perturbation. The studies described in Chapters 3 and 4 will demonstrate the effectiveness of these techniques as well as this general waveguide and sample design.

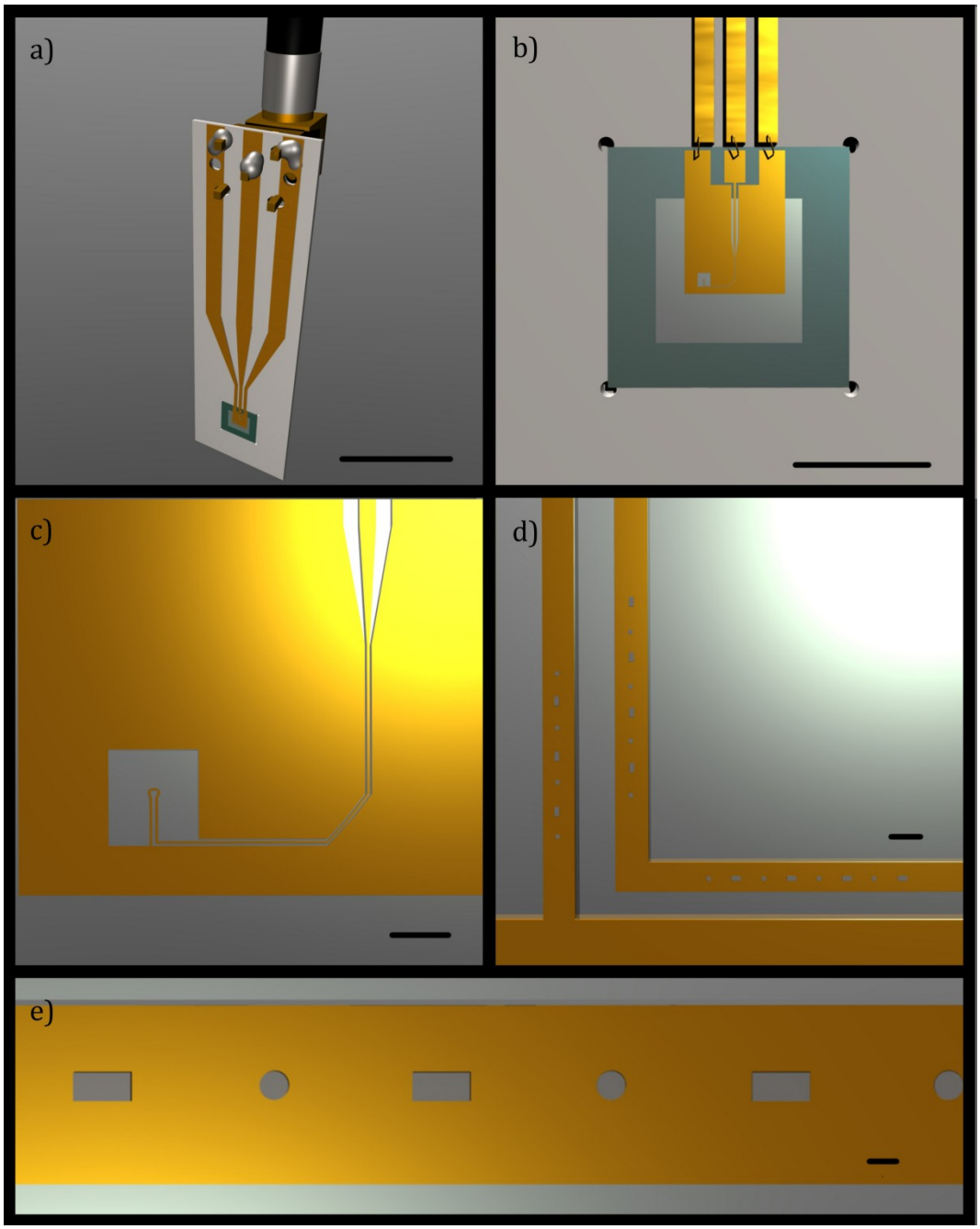

Figure 2.1 Samples for studying spin dynamics in confined geometries using soft x-ray transmission microscopy. Scale bars are as follows: a) 1.5 cm b) 2.5 mm c) 100 µm d) 10 µm and e) 2 µm. The patterned magnetic elements shown in e) were fabricated using e-beam lithography while the waveguides were fabricated using UV lithography.

2.1 Waveguide Fabrication

The microcoil design of the waveguide (Fig. 2.1(d)) allows for magnetic sample placement on either the waveguide, or between two wires of the waveguide. As such, the design is very general, providing the opportunity for studies applying a field in the plane of samples resting on the waveguides, or for studies applying a field normal to samples resting between two waveguide segments. In this dissertation the waveguide was used to apply magnetic fields in the plane of samples.

The key steps in the fabrication of the waveguides are depicted in Figure 2.2. Gold (Au) waveguides designed with a resistance of about 50 Ω were patterned onto silicon (Si) wafers which had 100 nm Si_3N_4, deposited through chemical vapor deposition. UV contact lithography was used to define the waveguides in positive tone resist which becomes soluble when exposed to a sufficient dose of radiation. The Au waveguides require a thin layer of titanium (Ti) as an adhesion layer[54]. A 5 nm Ti / 100 nm Au film was deposited over the patterned resist using e-beam evaporation. Next, the resist and the excess Ti / Au was stripped from the wafer. This liftoff process was done with the resist side down to minimize the chances of redeposition of the stripped materials. The waveguides are fabricated before the membranes, as rough agitation was required to achieve full liftoff and this would not have been possible if the delicate membranes were already defined.

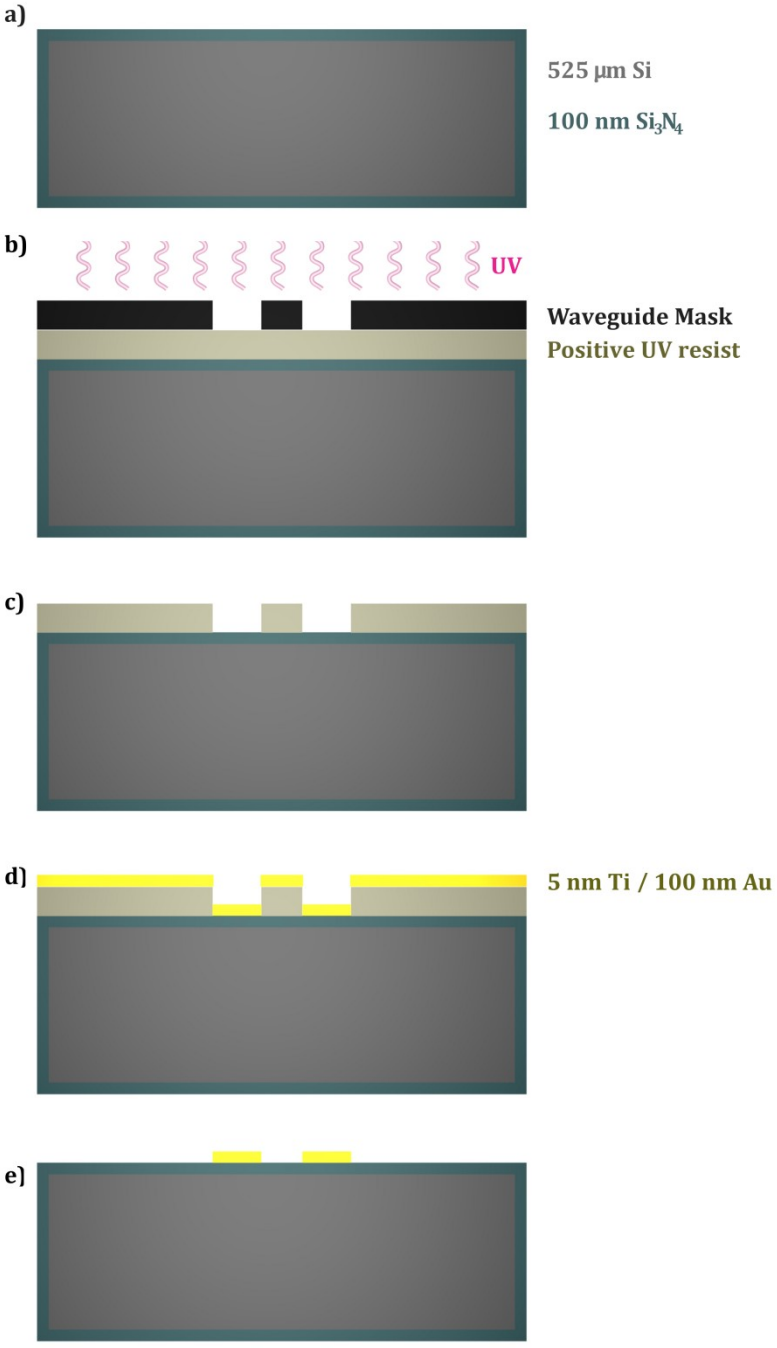

Figure 2.2 Waveguide fabrication. a) Starting substrate is a 4" diameter, 525 µm thick Si wafer with 100 nm low stress Si_3N_4. b) UV contact lithography, exposure of positive tone resist. c) Development of resist. d) E-beam evaporation of 5 nm Ti / 100 nm Au. e) Liftoff.

2.2 Membrane Fabrication

Si_3N_4 membranes were used as the substrate for the samples. Si_3N_4 is very transmissive at the energies needed for spin dynamics studies. At the Fe L_3 edge (707 eV), a 100 nm Si_3N_4

film will transmit about 82% of the incident photons[55]. Beyond its transmissive properties, Si_3N_4 greatly facilitates the fabrication process of membranes. In membrane fabrication, Si_3N_4 is not only used as a mask to the wet etch of Si, but also as an etch stop for the membrane, and as the membrane itself. In addition, by using low stress Si_3N_4, which is rich in Si, the membranes are relatively robust.

The key steps in the fabrication of the membranes are depicted in Figure 2.3. Si_3N_4 membranes which were 2.5 mm x 2.5 mm x 100nm were defined by etching the Si wafer from the back. UV contact lithography was used to define the membranes in positive tone resist. Before exposure with the UV radiation, the membrane mask was aligned to the waveguides using infrared light. Once the resist was developed and baked, it was used as a mask during the dry etching of the Si_3N_4. The Si_3N_4 was etched from the back, exposing regions of Si with a plasma etch using CHF_3 and O_2. With the Si_3N_4 patterned, it could be used as a mask during the wet etch of the Si in potassium hydroxide (KOH). Although Au is only slowly etched in KOH, Au layers can still be vulnerable to peeling in KOH. With the Au waveguides on the front of the wafer protected in a Teflon holder, a heated 30% aqueous solution of KOH was used to etch the Si wafer. KOH etches Si anisotropically, producing straight walls at a 54.74º angle as shown in Figure 2.3(d) [56].

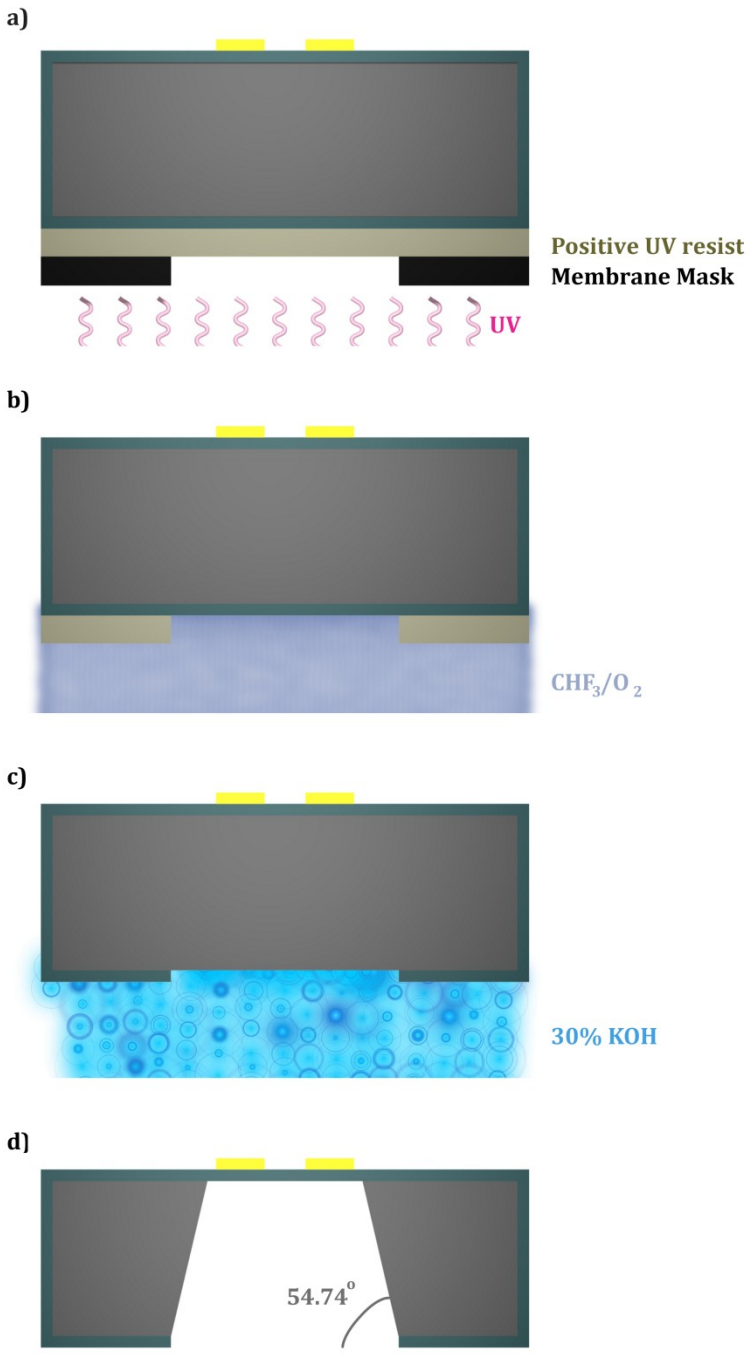

Figure 2.3 Membrane fabrication. a) UV contact lithography on back of wafer, exposure of positive tone resist. b) Development of resist and Si_3N_4 dry etching with CHF_3/O_2 c) Wet etching of Si with heated 30% KOH. d) After wet etch membrane has been defined. Frame has a 54.74º angle as shown.

2.3 Patterned Permalloy Fabrication

With the membranes and waveguides defined, the magnetic samples could be fabricated. The key steps in the fabrication of the magnetic samples are depicted in Figure 2.4. Depending on the experiment, various $Fe_{20}Ni_{80}$ shapes were patterned with areal dimensions on the order of

a micron and thicknesses of 45 nm or 100 nm. E-beam lithography was used to define the patterns in positive tone resist. Careful alignment between the pattern geometry and the waveguides was essential as an alignment error of a few microns could place the samples only partially on the waveguide. The $Fe_{20}Ni_{80}$ was deposited over the patterned resist using e-beam evaporation. Evaporation does not perfectly reproduce the stoichiometry of an alloy as each component has a distinct vapor pressure[54]. This is a disadvantage to using evaporation; however, for the purposes of these experiments, the composition of the deposited thin film remained close enough to the desired stoichiometry to not be a concern. An energy dispersive x-ray spectroscopy measurement of a $Fe_{20}Ni_{80}$ film deposited with the e-beam evaporation system used to fabricate the samples, revealed a composition which was roughly 18% Fe, 82% Ni. After deposition of the $Fe_{20}Ni_{80}$ film, the resist and the excess $Fe_{20}Ni_{80}$ was stripped from the wafer. This liftoff process was facilitated with gentle agitation and with the resist side down to minimize the chances of redeposition of the stripped materials.

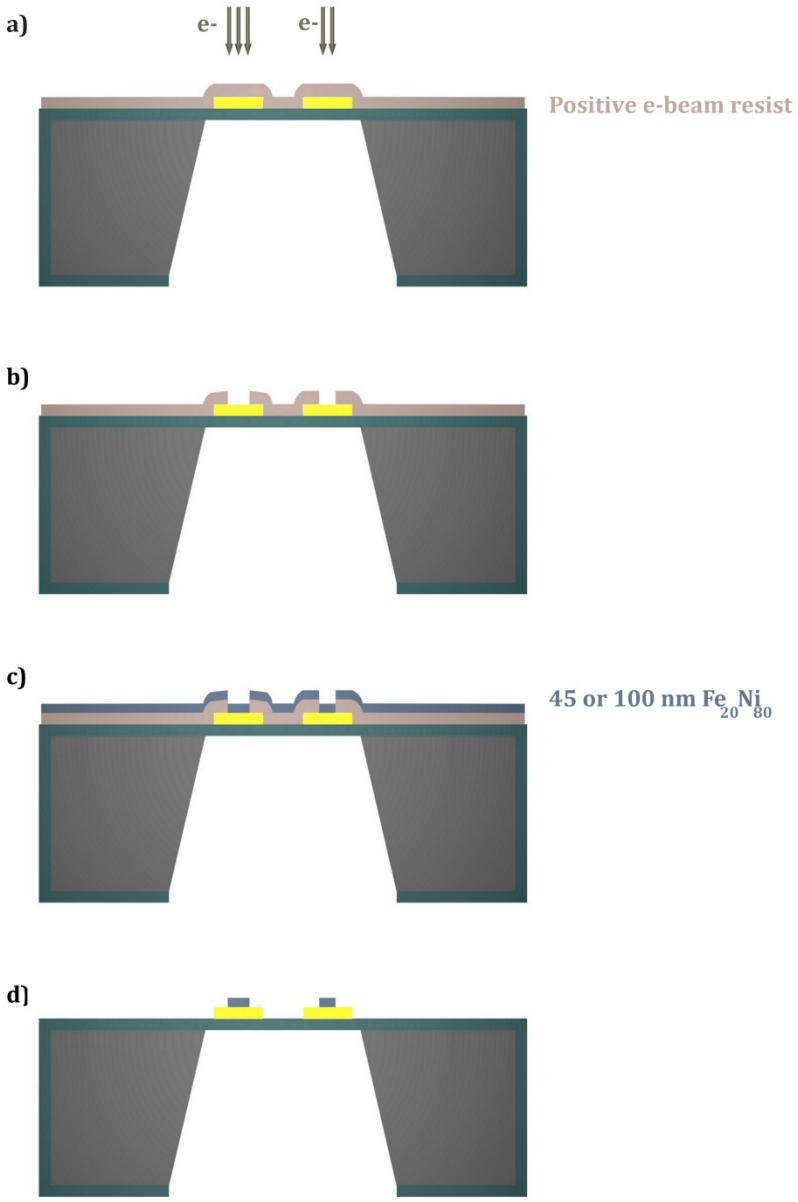

Figure 2.4 Patterned $Fe_{20}Ni_{80}$ fabrication. a) E-beam lithography, exposure of positive tone resist. b) Development of resist. c) E-beam evaporation of 45 nm or 100 nm $Fe_{20}Ni_{80}$. e) Liftoff.

2.4 Preparing Samples for XM-1

To see the full final sample configuration, refer to Figure 2.1. After fabrication individual sample substrates measuring 5 mm x 5 mm with 2.5 mm x 2.5 mm membranes, were glued into circuit board holders. The waveguides on the Si frame were wire bonded from pad structures to the circuitry on the board. A standard RF coaxial connector, a SMA connector, was mounted onto the board to allow current to be applied through the waveguides. With this configuration the samples were prepared for any of the experimental techniques outlined in the rest of this chapter. The circular sample shown in Figure 2.5(a) had a diameter of 2 μm and a thickness of 100 nm and was used in the experiments outlined in Chapter 3, and the rectangular

sample shown in Figure 2.5(b) had areal dimensions of 2 µm x 4 µm and a thickness of 45 nm and was used in the experiment discussed in Chapter 4.

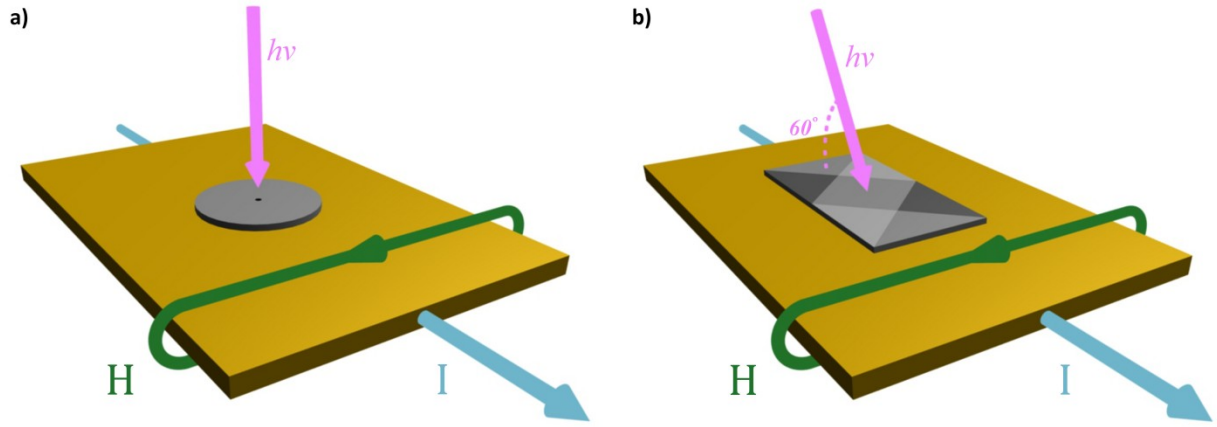

Figure 2.5 Patterned samples on waveguides with applied Oersted fields. Incident photons are perpendicular to the sample plane in a) and provide images with out-of-plane magnetization information. Incident photons are at a 60 degree angle to the sample plane in b) and provide images with in-plane magnetization information.

2.5 Dynamics Studies at XM-1 without Time Resolution

Currently, time-resolved experiments at XM-1 can only be run a few weeks out of the year in a special operational mode of the ALS (two-bunch mode). However, non time-resolved experiments can provide useful information about spin dynamics and have some advantages over time-resolved studies such as speed of image collection and lower image noise. In normal operation of the ALS, the x-rays are generated by hundreds of bunches of electrons circling the synchrotron storage ring. This provides almost continuous illumination with only 2 ns between each x-ray pulse. With this illumination, images can be taken in a few minutes or less and have very low noise.

In Chapter 3 the response of a vortex core to external oscillating fields is investigated with both non time-resolved imaging and time-resolved imaging with a resolution of about 70 ps. This study required a large survey of RF field frequencies and amplitudes which would not have been practical during time-resolved experiments. The frequency where the vortex core experienced resonant motion was particularly important. While the resonant frequency can be predicted fairly well using theory[57], actual sample resonant frequencies can be as much as 30% off of the theoretical resonant frequencies[28]. Thus, locating the resonant frequency of the specific sample under investigation before time-resolved experiments are in progress can save a good deal of experimental time. Such a method was developed and used for the experiments in Chapter 3.

The non time-resolved dynamics experiments in Chapter 3 were performed by imaging the vortex core, and watching for frequencies and amplitudes of the applied field which caused the vortex core image to change. Specifically, the vortex core would blur or disappear, which indicated motion of the vortex core or vortex core polarity flipping or both as is described in more detail in Chapter 3.

2.6 Dynamics Studies at XM-1 with Time Resolution

The time-resolved experiments described in Chapters 3 and 4 were done at XM-1 during the two-bunch mode operation of the ALS. In two-bunch mode, two electron bunches traverse the synchrotron storage ring separated by 328 ns. This produces x-ray pulses with a frequency of about 3MHz and durations of about 70ps. The width of the electron bunches determines the duration of the emitted x-ray pulse and therefore sets the time resolution of these experiments. The frequency of the x-ray pulses sets the experimental clock. The intensity of a single x-ray pulse, which is only a few photons, is not enough to generate a single-shot image at current synchrotron experiments, such as magnetic microscopy at XM-1; however, by accumulating the transmitted x-rays from many pulses, one can record an image of the sample. For a single x-ray image about $10^{10\text{-}11}$ photons are needed, taking into account about 1000 photons per CCD pixel, 1000 x 1000 pixels, and a typical 10% efficiency for each of the x-ray optics. To accumulate sufficient x-rays for an image, the dynamic process of interest must to repeat perfectly about 10^8 times as the sample must be in exactly the same configuration for each of the x-ray pulses. In addition, the sample dynamics must be carefully synched to the x-ray pulses to ensure that the spin configuration is in the same state each time the x-rays are incident on the sample.

In the following sections two different techniques for matching the spin dynamics to the imaging x-rays are discussed. First, a phase-locking technique which keeps a continuous oscillating applied magnetic field in perfect phase with the x-ray pulses is described, and second, a stroboscopic pump-probe technique which pumps the sample repeatedly with a fast magnetic field pulse before each probing x-ray pulse is described.

2.6.1 Phase Locking Experimental Technique

A diagram of the phase-locking experimental setup is shown in Figure 2.6, where an RF field is applied to a magnetic sample in phase with the x-ray pulses. In this type of experiment the perturbation of the magnetization is continuous, but, as the dynamic response of the spins to the oscillating field is expected to vary over a period of the field oscillation, the phase of the RF field must be locked to that of the x-rays. This phase-locking is accomplished with a feedback loop where the clock signal from the synchrotron is used as a reference frequency. Different stages of the dynamic response of the sample can be studied by changing the phase shift between the oscillating magnetic field and the x-ray pulses.

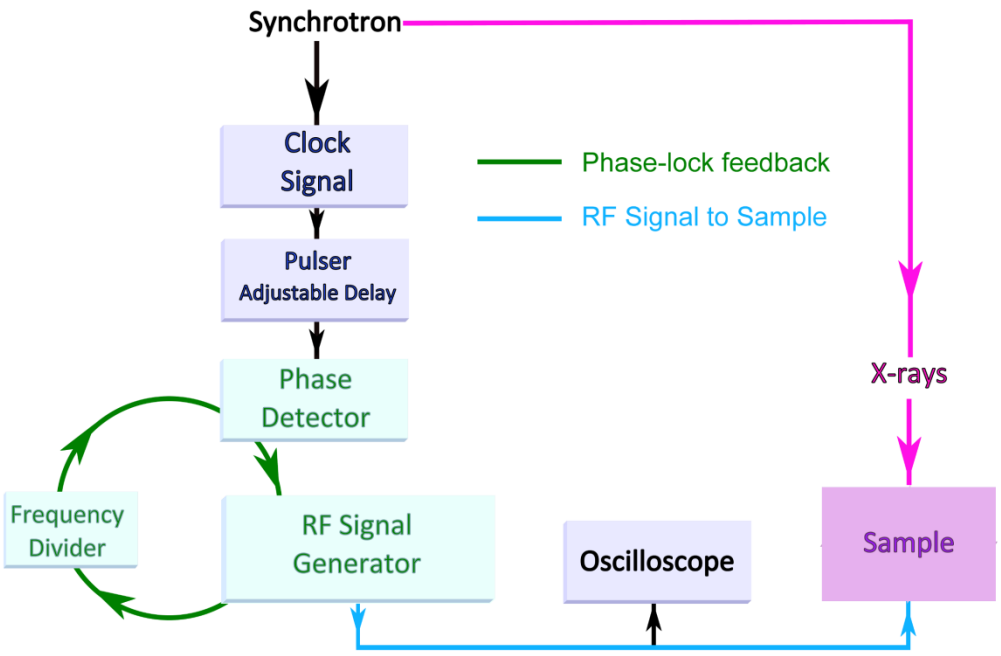

Figure 2.6 Signal flow diagram for the phase-locking experimental setup at XM-1. Figure following [44].

2.6.2 Pump and Probe Experimental Technique

In pump-probe experiments, the goal is to excite the sample and watch the dynamics before the sample relaxes back to its initial state. For spin dynamics studies, the rise time of a pumping field pulse must be very fast so that the magnetization cannot adiabatically follow the pulse. For the experiment described in Chapter 4, a fast electronic pulse with a rise time of about 100 ps was generated by a pulser at 3MHz and launched into the waveguide structure to generate an Oersted field pulse. A typical field pulse is shown in Figure 2.7. The phase of the pulse is linked to the synchrotron by using the clock signal from the synchrotron as the trigger for the pulse. The evolution of the dynamics could then be studied by varying the delay time between the excitation pump pulse and the x-ray probing pulse.

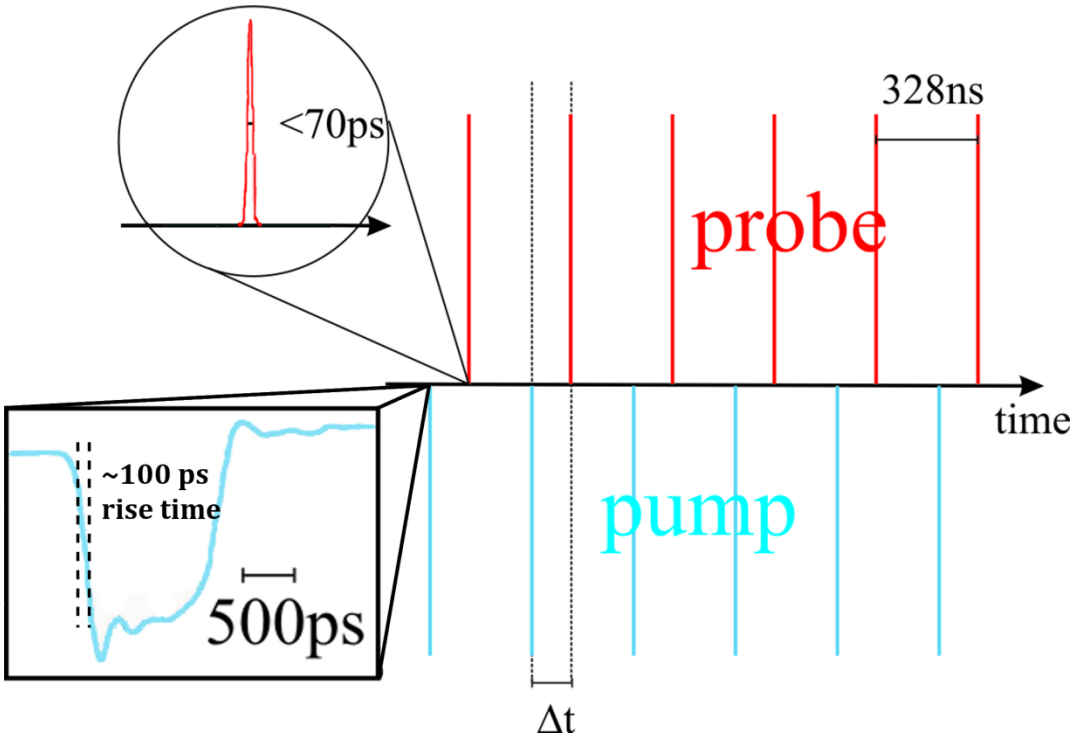

Figure 2.7 Pump and probe scheme used to image spin dynamics with soft x-ray microscopy. The probing x-ray pulse has a width of 70ps and a 3MHz frequency. By shifting the time difference between the arrival of the pump and probe, images can be taken of the magnet. Figure from [53].

A diagram of the pump-probe experimental setup is shown in Figure 2.8. The critical issue in the signal flow of this technique is setting the time delay between the pump and probe. The x-ray pulses are separated by 328 ns, and if not carefully arranged the pumping field pulse could arrive at the sample too early for the dynamic response to be seen with the x-rays. To determine an absolute time scale, where time zero is defined to be the arrival time of the x-rays onto the sample, an electronic signal of an avalanche photodiode (APD) located close to the sample and triggered by the arriving x-ray pulse is used. The APD signal and the pulse could be simultaneously monitored with the fast oscilloscope. A digital delay line allowed the pump signal to be delayed up to a full 328 ns in 2 ns steps with an accuracy of 10 ps. Thus the whole time span between subsequent x-ray pulses can be addressed.

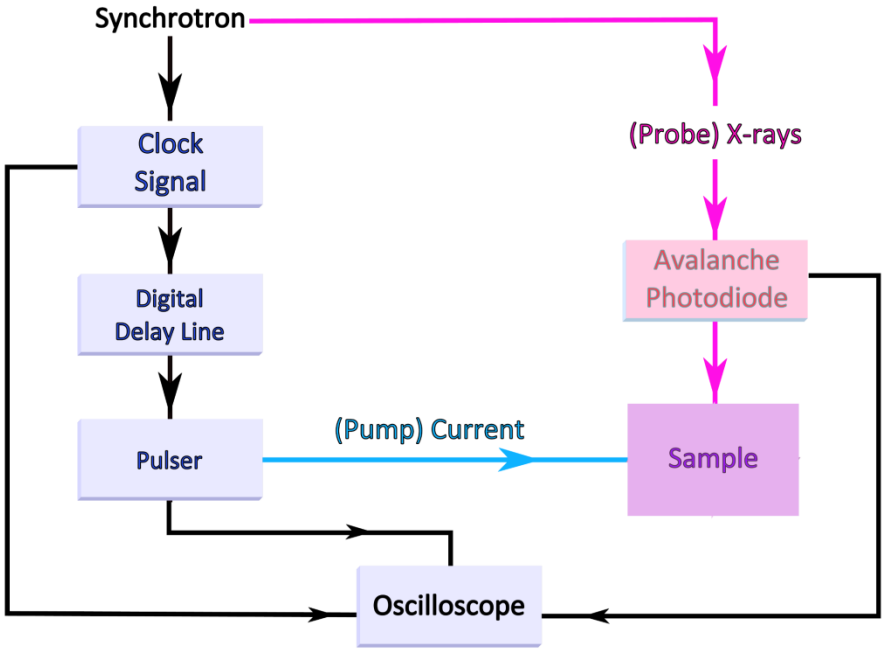

Figure 2.8 Signal flow diagram for the pump and probe experimental setup at XM-1. Figure following [53].

The three experimental techniques described in this chapter provide a variety of options for spin dynamics studies. The non-time resolved technique is especially useful for investigations requiring the testing of many different parameters. As long as the feature of interest is clearly resolvable when no dynamics are occurring, a change in the feature, or complete disappearance, under specific conditions provides a strong indication of dynamics. As shown in Chapter 3, section 3.1, such investigations can reveal interesting new spin dynamics behaviors.

The time-resolved techniques at XM-1 have a resolution of 70 ps and as such are an excellent probe of domain wall and vortex core motion in response to an applied magnetic field. The phase-locking technique allows the continuous periodic response of a spin system to an oscillating field to be studied, as will be seen in Chapter 3, section 3.2. The pump-probe technique allows the repeated excitation of a spin system from a single fast rising magnetic field pulse to be studied, as will be seen in Chapter 4.

Chapter 3 Spin Dynamics: Resonant Vortex Core Motion

Magnetic vortex cores are one of the most remarkable magnetic configurations and are currently attracting considerable interest; their dynamics are interesting from a fundamental viewpoint[58-60], and in addition, they may have future application in technology[24,61]. This chapter details two studies on resonant vortex core motion. The first study uses time-averaged, or non time-resolved, imaging to survey the reaction of the vortex core to various driving fields with frequencies of several hundred MHz. This survey revealed a nonlinear response of the vortex core for high amplitude fields. The second study uses time-resolved imaging in an attempt to make detailed observations of the vortex core trajectory when an RF field is applied; however, the spatial resolution of the experiment is insufficient to resolve these details. The chapter closes by outlining the experimental improvements needed for further investigations.

Vortex cores exhibit a gyrotropic motion under an applied RF field that depends on the polarity of the vortex core[5], where the resonant frequencies are usually several hundreds of MHz [57-58]. This circular motion of the core around its original location can be excited by both magnetic fields and electric currents[57-60]. The gyrotropic motion of the vortex core, while reasonably well understood[54,57], has yet to be fully investigated experimentally[28,59]. Moreover, the resonant gyrotropic vortex core motion may be relevant to future technological applications. The stability of a magnetic vortex core makes it an interesting candidate for information storage, but also raises the issue of how to efficiently manipulate the state of the vortex core, something that may be achieved by first triggering gyrotropic motion[26-27].

This chapter describes experiments looking to further our understanding of the gyrotropic motion of the vortex core. A thin cylindrical $Fe_{20}Ni_{80}$ sample with a radius of 2 μm and a thickness of 100 nm is studied as oscillating fields with varying amplitude and frequency are applied. The resonant response of the vortex core is verified and examined as the amplitude of the applied field is increased. For high enough applied fields, the character of the vortex core response changes notably, with the single resonance of the vortex core apparently splitting into two distinct resonances[62-63]. In addition, at lower amplitude fields, where the response remains

linear, the vortex core trajectories are studied. It has been predicted in theory that the vortex core motion, circular at resonance, will become more elliptical in nature as the driving frequency is set just above and below resonance[59]. Time-resolved images of the vortex core dynamics provide an opportunity to examine the trajectories of the vortex core in detail.

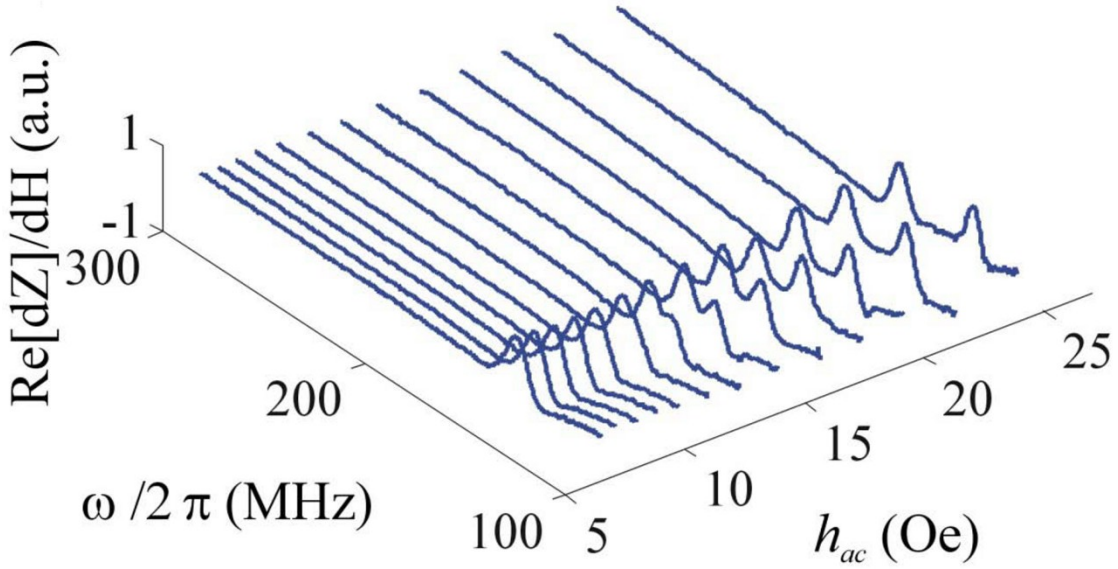

Figure 3.1 Real part of the impedance derivative vs. frequency of h_{ac} for various amplitudes of h_{ac}. Data from an array of 2 µm x 1 µm x 40 nm ellipses with a 60 Oe applied static field. The single resonance peak at lower amplitude fields appears to split into two resonances at higher amplitude fields. Figure from [62].

3.1 Nonlinear Resonant Vortex Core Motion

In a study of the gyrotropic motion of the vortex core by K. Buchanan et al., an apparent nonlinear response was recorded (Fig 3.1)[62]. The unexpected response of two resonant peaks at high amplitude applied fields could not be fully explained by theory. The vortex core is generally predicted to have one resonance that is related to the geometry of the magnetic sample with the vortex core[57]. This result can be seen to emerge from the Thiele equation which is commonly used to describe the motion of the vortex core and is written as[64]:

$$-\vec{G}\times\frac{d\vec{X}}{dt}-D\frac{d\vec{X}}{dt}+\frac{\partial W(\vec{X})}{\partial\vec{X}}=0 \qquad (3.1)$$

Here, $\vec{X}$ is the displacement of the core and the relevant vectors are shown in Figure 3.2. The first term in the Thiele equation describes a Magnus type force, the gyroforce, which causes a spiral type motion of the core. The gyrovector can be defined as $G=\frac{2\pi LM_s}{\gamma}p\hat{z}$, where p is the vortex core polarity, L is the sample thickness, M_s is the saturation magnetization, and γ is the gyromagnetic ratio.

The second term of the Thiele equation describes the damping of the motion, where D is the damping coefficient. The final term describes the motion of the core in the energy potential

$W(\vec{X})$, largely determined by the magnetostatic energy which is minimized when the core is centered in the structure and there are no stray fields.

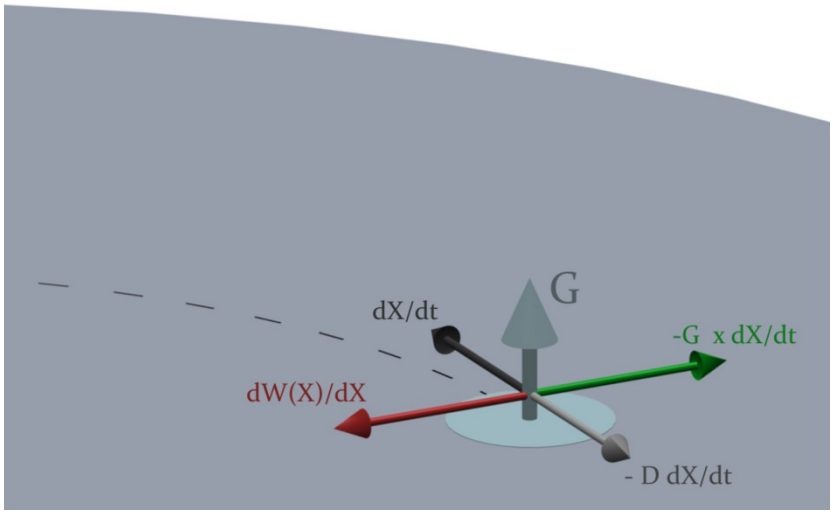

Figure 3.2 Gyrotropic vortex core motion as described by the Thiele equation.

Approximating $W \propto \frac{1}{2}\kappa X^2$, observing $\vec{G} \times \frac{d\vec{X}}{dt} = G\omega\vec{X}$, and neglecting the damping term, we see that equation 3.1 leads to:

$$G\omega\vec{X} - \kappa\vec{X} = 0 \tag{3.2}$$

Thus we find that the resonant frequency $\omega_0 = \kappa/G$. Experiment has been found to agree very well with this simple theory[57-58,60]. Further examination of the gyrotropic vortex core motion is needed to understand the apparent nonlinear results found by K. Buchanan et al.

The experiment described in this section attempts to understand the resonance behavior at high amplitude applied fields through x-ray imaging. Frequencies applied to the sample ranged between 200 MHz to 500 MHz, and amplitudes of 4 Oe, 8 Oe, and 10 Oe were applied. This study was done without time resolution as described in section 2.5 and images were taken using 707 eV (1.75 nm) radiation, which corresponds to the Fe L_3 edge. In order to directly image the vortex core, images were taken with the sample positioned perpendicular to the x-ray beam direction, allowing specifically the out-of-plane magnetization to be imaged (Fig. 2.5(a)). While the images were taken without time resolution, dynamic behavior of the vortex core could be detected by watching for changes in the time averaged images. This technique allowed for a large number of frequencies to be probed for each amplitude applied.

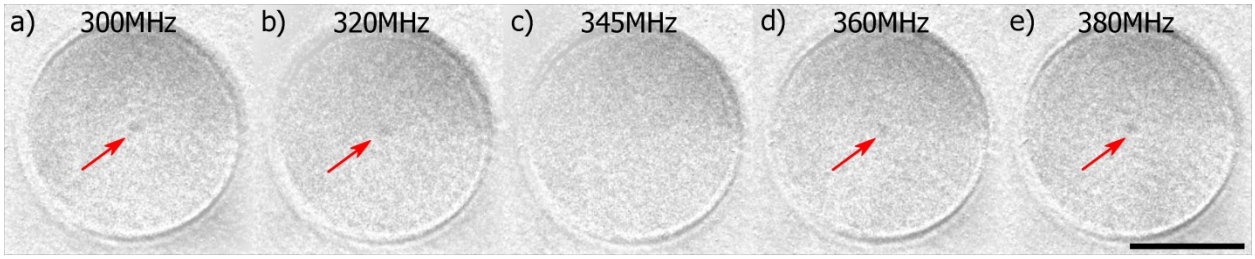

Figure 3.3 A representative sequence of images taken with a lower amplitude oscillating field with $H_0 \sim 4$ Oe. Sample imaged at (a) 300 MHz, (b) 320 MHz, (c) 345 MHz, (d) 360 MHz, and (e) 380 MHz. Red arrows highlight the images of the dark vortex core. The vortex core is not visible in (c). Each displayed image is a difference image, formed by dividing two images taken with opposite polarizations. Such an image set took about 2 minutes to record. Scale bar is 1 μm.

3.1.1 Nonlinear Resonant Vortex Core Motion: Results from XM-1

A set of images taken with a lower amplitude, 4 Oe, field applied to the sample is shown in Figure 3.3. The image contrast of the vortex core was enhanced by taking images with opposite helicities and dividing the two, providing images with the core clearly shown as a dark or bright spot in the sample. The vortex cores can be seen in most of the images, appearing as dark spots at the center of the disk. As can be seen in Figure 3.3(c), the vortex core is not discernable at all frequencies; this helps pinpoint the frequencies at which the vortex core has a dynamic response. The core disappearance could have several causes. The core would be expected to blur if it was in motion, spreading out the XMCD signal until it could not be resolved, or if the core polarity was rapidly flipping, averaging out the dark and light contrast into a gray background, or if both lateral motion and polarity flipping was occurring. This disappearance, or blurring, of the core image, was observed repeatedly at certain frequencies. It should be emphasized that this was a reproducible and repeatable effect and we can thus infer that the core blurring was caused by a change in the magnetization of the sample rather than some type of experimental artifact.

Examining Figure 3.3, there appears to be a dynamic change in the core around 345 MHz. This is about 0.7 times the expected resonant frequency for samples of these dimensions[57]; other experiments studying gyrotropic vortex motion have seen similar deviations from calculation[28]. This indicates that what we are observing in Figure 3.3 is in fact resonant gyrotropic motion, causing the image of the core to blur to gray in Figure 3.3(c).

In addition to imaging the vortex core response to different frequencies, magnetic fields of several amplitudes were applied to the sample (Fig. 3.4). We see for an applied field with an amplitude of about 8 Oe, the frequency range where there are core dynamics appears to broaden slightly; but for the most part there is little change in the sample behavior. A significant change is seen around 10 Oe where there appear to be two distinct regions of dynamics. A sequence of images at this amplitude is shown in Figure 3.5. Importantly, we are able to image the core near 345 MHz while at 320 MHz and 360 MHz the core is not visible in the images. This indicates that dynamic behavior is now occurring on either side of the original resonance frequency. In addition, the image of the core at the original resonance frequency indicates that the core is not changing or moving between the two areas of dynamics.

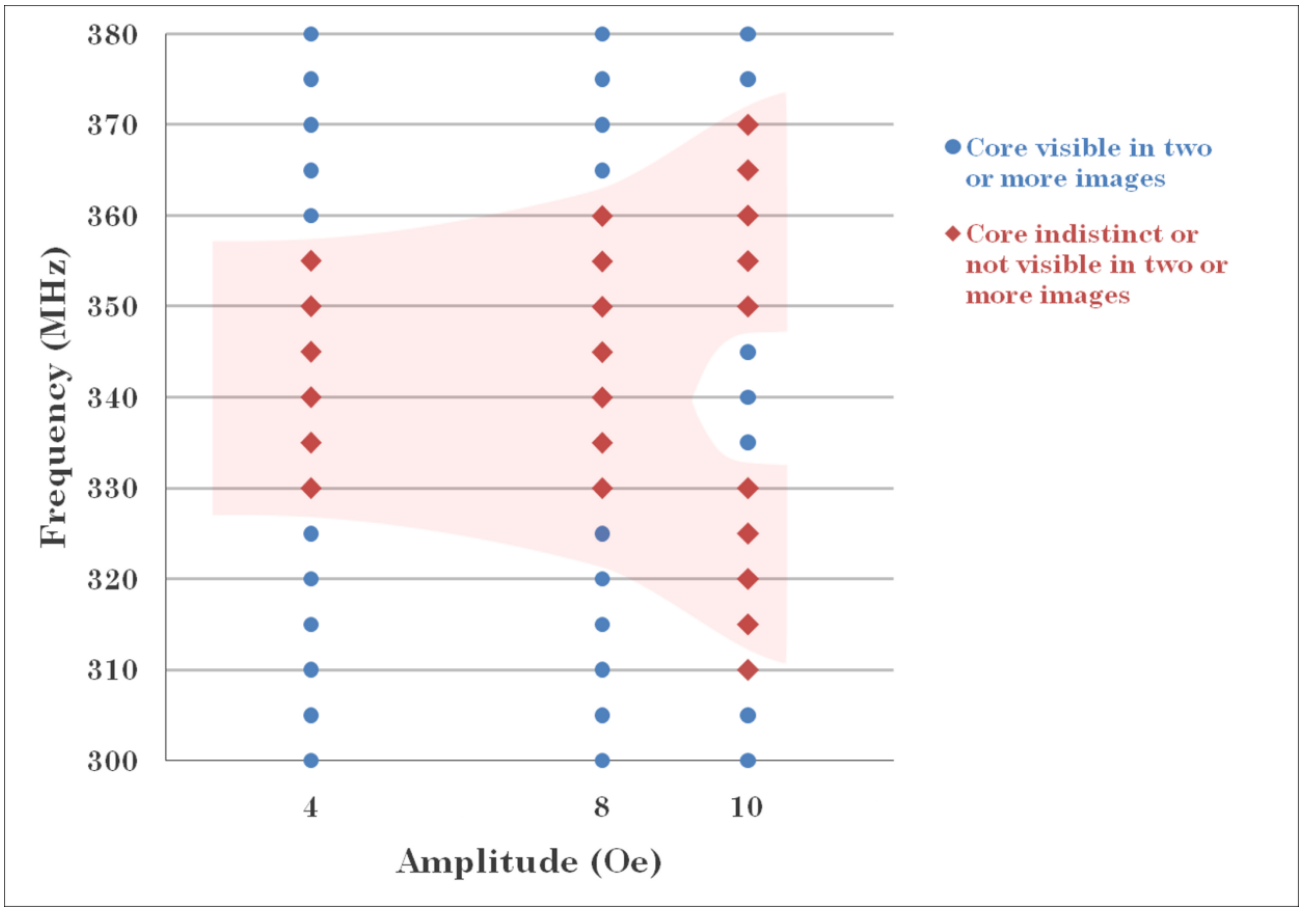

Figure 3.4 A summary of the images taken over a range of frequencies and amplitudes. The blue circles indicate a frequency and amplitude where the core was visible, and the red diamonds a frequency and amplitude where the core was indistinct or not visible in at least two images. The pink overlay emphasizes the general trend of the data: a single resonance splitting to two at higher applied fields.

We see in Figure 3.5(c) that the vortex core is bright rather than dark, indicating that the core polarity switched during the dynamics at frequencies before and after the stable image at 345 MHz. The core may have flipped polarity just once during the dynamics, or may have been rapidly flipping polarity continually, ending by chance with a dark contrast. The core images at the highest and lowest frequencies were sometimes white and sometimes black, supporting the latter possibility. There was no switching of polarity observed when changing between frequencies where the core could be clearly imaged. Interestingly, the core was always white in images between the frequency ranges where dynamics occurred. It is difficult to determine if this was simply a random chance or if it was a real effect as the full frequency range response was imaged with a 10 Oe RF field only six times due to time constraints. It should also be noted that while core polarity flipping was certainly occurring as part of the dynamic response to the 10 Oe RF field, other dynamic processes may also have occurred. The images with the indistinct core could be the result of core motion and switching.

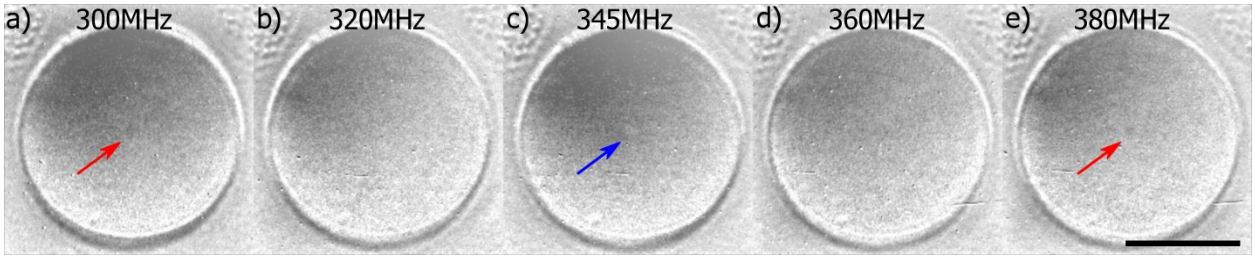

Figure 3.5 A representative sequence of images taken with a higher amplitude oscillating field with H_0~10 Oe. Sample imaged at (a) 300MHz, (b) 320MHz, (c) 345MHz, (d) 360MHz, and (e) 380MHz. Arrows highlight the visible vortex core in (a), (c), and (e). The red arrows point toward a dark vortex core while the blue arrow points out a light vortex core in (c), indicating a change in core polarity before and after the 345MHz image was taken. Each displayed image is a difference image, formed by dividing two images taken with opposite polarizations. Such an image set took about 2 minutes to record. Scale bar is 1 μm.

3.1.2 Nonlinear Resonant Vortex Core Motion: Discussion and Conclusions

Our observations suggest there are two resonant frequencies of the vortex core when relatively large amplitude RF fields are applied. This appears to confirm the findings of K. Buchanan et al.; however, the question of the origin of this nonlinear behavior remains open. While $W(\vec{X})$ is usually approximated to be proportional to $\vec{X}^2$ [60], a more precise description of the potential would include higher order terms[65-66]. It was suggested previously[62] that nonlinear vortex core behavior could be explained by higher order terms in the vortex potential. In this previous work the authors found that a crossover behavior of the amplitude could be achieved in numerical calculations, although the necessary parameter values required to achieve this effect could not be justified physically[62].

Recently, theory has been further developed to explain the spectra seen in Figure 3.1[67]. It has been postulated that the minima in the spectra separating two resonance peaks are an experimental artifact of fast core flipping, and not in fact regions where the core is motionless. The fast core flipping would be a result of a physical limit of the core motion being reached. An ultimate limit on the velocity of the vortex core has been calculated by K.-S. Lee et al.[68]; this critical velocity should impose a critical displacement of the core as well. As the core is expected to have a larger displacement with a larger applied field, a field large enough to push the core past its critical displacement could cause instability and thus fast vortex core flipping. During this fast vortex core flipping it is predicted that the core would have a circular spiral outwards, then a flip in polarity with a reduction in displacement, another spiral outwards, and so on. The model which describes this behavior predicts a general broadening of the frequency range of dynamics with increased amplitude of the driving field. This aspect of theory fits well with the experimental results summarized in Figure 3.4. A key difference, however, between theory and experiment is the image of the vortex core seen in Figure 3.5(c). The core should not be possible to image if it was in motion or flipping, or both as suggested by the theory. There is a chance that the white "core" imaged in Figure 3.5(c) is an artifact of the theorized fast core flipping motion; however, this is unlikely. The dynamics would need to have some type of non uniformity to result in a net white core when the core is suspected of flipping between black and white. It is much more likely that the core is in fact static.

Further work is needed to fully explain the results shown here. It would be beneficial to repeat this experiment; the more times the full frequency and amplitude range response can be

imaged, the clearer the vortex core behavior will become. For example, if further experiments also show only a white "core" before and after dynamics, it should be more seriously considered that the white "core" is a real artifact from some new type of dynamics response such as fast core flipping. Duplication of the experiment with a different sample could also confirm that the apparent nonlinear behavior was a general effect and not specific to a particular sample. In addition, a distinction between motion and core flipping might be made if a very stable magnetic contrast could be achieved in the images. In the present configuration, the contrast from the XMCD effect can be unstable because it relies on a particular portion of the x-ray beam selected by the optics. Changes in the beam section, due to changes from the synchrotron beam and due to minute drifting of the microscope components, can adversely affect the magnetic contrast. A slight decrease in image contrast quality might make a blurred core appear to have completely disappeared. This is relevant because ideally a blurred core image would indicate a gyrotropic motion and an image without any core would indicate a flipping of the core polarity. Using the present configuration of the microscope, a trend in the experimental data was clear; however, more information could be gained with more stable contrast.

The data described here show interesting behavior of the vortex core. The dynamic response of the core for high amplitude RF fields shows distinct nonlinear character. The modesplitting observed could be related to a critical displacement affecting the core dynamics, or could be due to a nonlinear vortex core potential; however, more experimental and theoretical work is needed to explain this behavior.

3.2 Time-Resolved Resonant Vortex Core Motion

Recently there has been considerable interest in observing vortex core trajectories during gyrotropic vortex core motion[69-70]. Understanding the trajectories of vortex cores allows for comparison with current theory and models and thus a deeper understanding of the energies involved with the displacement of magnetic spins. Such understanding will be crucial for any type of future spintronics technologies, whether it involves manipulating domain walls[70] or controlling vortex core polarity[24]. While the frequency response of a vortex core, as shown in the previous section, can be studied with non time-resolved x-ray imaging, a more detailed investigation into the dynamic behavior of vortex cores requires time-resolved experiments.

A detailed theoretical study of the vortex core response to oscillating fields has been carried out by K.-S. Lee et al.[60]. In this work the authors find that while the trajectory of the vortex core on resonance is circular, it becomes increasingly elliptical off resonance (Fig 3.6). At frequencies above resonance, the trajectory is elongated in the direction of the applied field, and at frequencies below resonance, the trajectory is elongated normal to the direction of the applied field. Confirming these predictions is an experimental challenge as the excursion of the vortex core is vastly reduced off-resonance. Examining Figure 3.6, one can see that the theoretical trajectories off-resonance are for an applied field with twice the amplitude as that for the trajectory on-resonance. Practically, an experiment probing $\omega_H/\omega_D \sim 0.9$ and 1.1 is feasible.

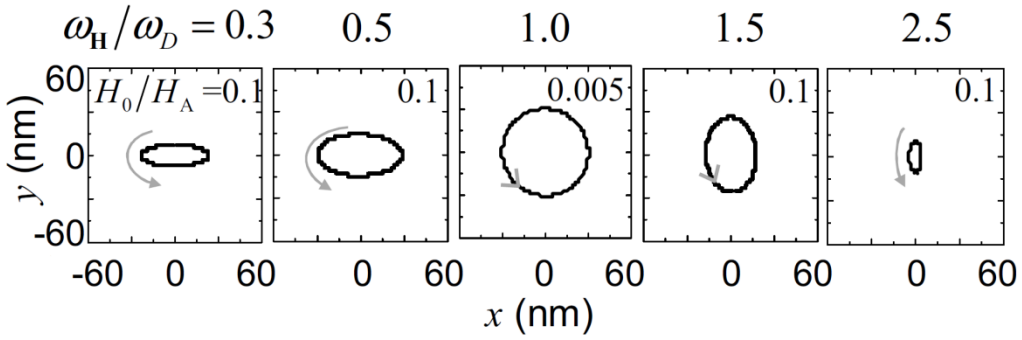

Figure 3.6 Theoretical trajectories of vortex core in response to applied RF field with frequency ω_H and amplitude H_0. Resonance frequency is ω_D and H_A is 500 Oe. Figure is from [59].

In the experiment described in the following pages, the behavior of the vortex core is examined at resonance and very near resonance in an attempt to observe a transition to elliptical motion as the driving field is moved off-resonance. This experiment also provided an opportunity to test the validity of the time averaged, or non time-resolved, technique used in the previous section as the same $Ni_{80}Fe_{20}$ sample was used in both experiments. Time-resolved images were taken using the phase-locking experimental technique described in section 2.6.1 and images were taken again at the Fe L_3 edge. The time resolution was 70 ps. As in the previous section, images were taken with the sample positioned perpendicular to the x-ray beam direction, allowing specifically the out-of-plane magnetization to be imaged (Fig. 2.5(a)).

3.2.1 Time-Resolved Vortex Core Trajectories at Resonance

A pair of images of the vortex core taken with time resolution is shown in Figure 3.7. The image contrast of the vortex core was enhanced by taking images with opposite helicities and dividing the two. The shift of the vortex core can be seen from upper left in the first image, to lower right in the second image, where the applied field phase shift between the two images was 1 ns. The RF field applied to the sample here had a frequency of 350 MHz and an amplitude of 4 Oe. This is an important confirmation of gyrotropic motion occurring at the resonance detected in the non time-resolved experiment, 345 MHz. While the RF field was generated with different electronics for the two experiments, and thus was not identical, the amplitude of the field generated in this time-resolved technique was very close to that generated in the lowest amplitude runs in the non time-resolved technique. Both had an amplitude of roughly 4 Oe, where this was calculated using the Biot-Savart law to convert an applied peak-to-peak voltage to a magnetic field.

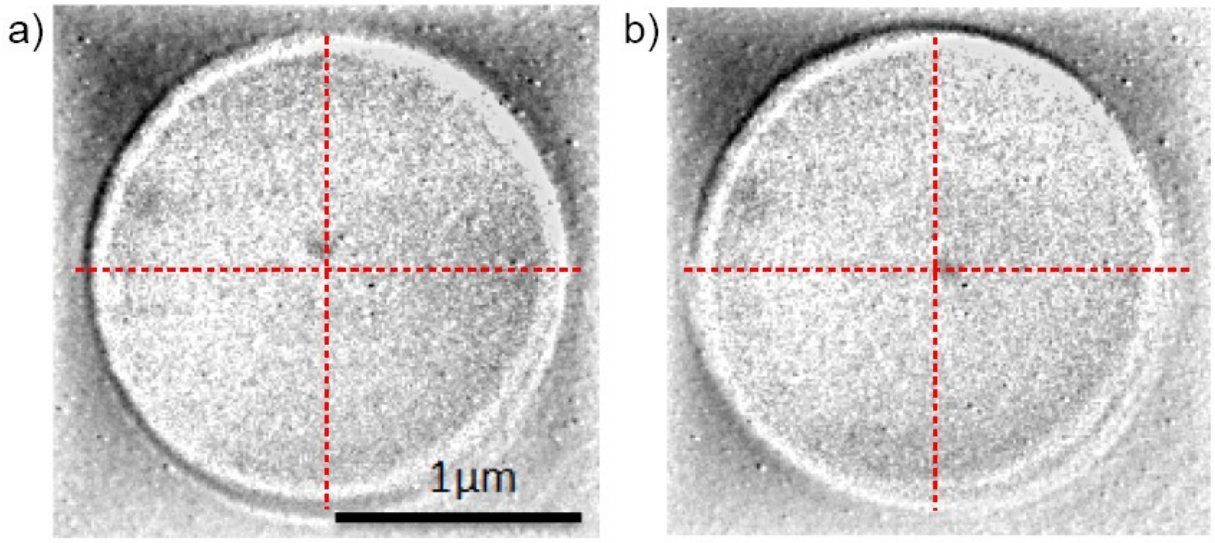

Figure 3.7 Representative time-resolved images of the vortex core. The phase delay is 0 ns in (a) and 1 ns in (b). The applied field had a frequency of 350 MHz and an amplitude of 4 Oe. Dotted red lines are used as reference to underline the shift of the vortex core. Each displayed image is a difference image, formed by dividing two images taken with opposite polarizations. Such an image set took about 20 minutes to record.

Further analysis of the core motion was possible by recording for each phase delay the position of the vortex core in relation to the top and right edges of the sample. A plot of the core trajectory where a driving field with a frequency of 350 MHz and amplitude of 4 Oe has been applied is shown in Figure 3.8. The trajectory shown is consistent with theory[57,59] and other experiements[69]. Theory predicts a circular trajectory with a radius of about 5 % of the radius of the sample[57], which for this experiment would be about 50 nm and is within the standard limits of resolution for XM-1 (see section 1.2.2). The trajectory shown here is on the order of magnitude of this expectation, as were the rest of the trajectories which ranged between 50 and 100 nm.

3.2.2 Extending the Vortex Core Trajectory Analysis

A summary of the vortex core trajectories observed is shown in Figure 3.9. Here, each plot of the vortex core positions, like that shown in Figure 3.8, was fitted to an ellipse. The radii of the ellipse were then used as coordinates for the plot in Figure 3.9. From such a graph we would expect from theory to see trajectories of cores driven above the resonant frequency to be elongated on the vertical axis, and those of cores driven below the resonant frequency to be elongated on the horizontal axis. From this data such a trend is not evident.

The error bars for the determination of the trajectory dimensions as shown in this figure are quite large and the data point distribution falls within the error bars. The large error is the result of combining multiple uncertain elements to get the final calculation of the trajectory radii. Two measurements are required to determine the core position: a reference pixel readout of a sample edge, and the pixel readout of the core center itself. In addition, an ellipse must be fitted to these points, with a large difference in ellipse parameters between fits of the minimum and maximum spread of the points.

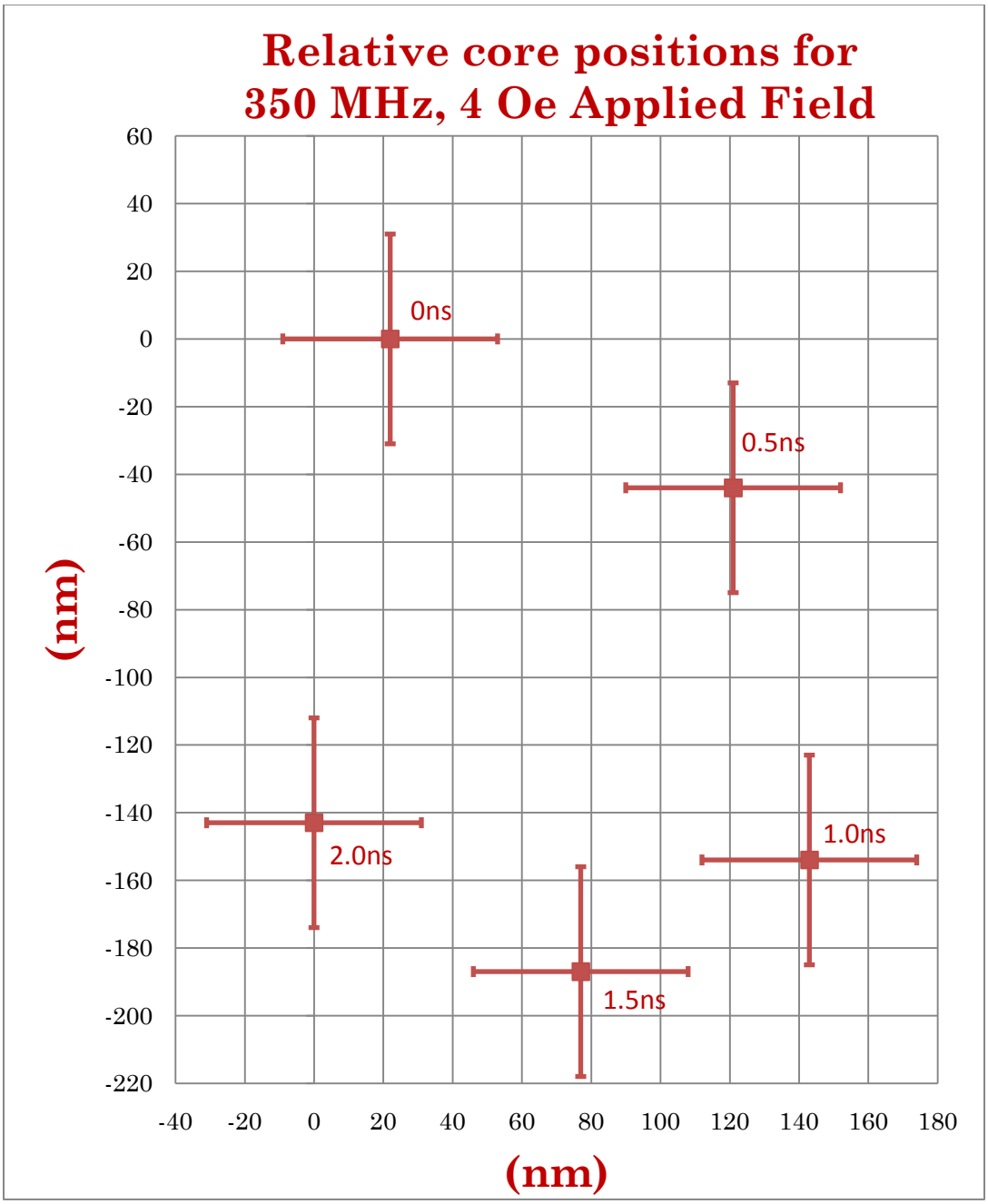

Figure 3.8 Sample plot of vortex core trajectory determined from time-resolved images. Distances are relative and plot origin is simply set to the largest y position and smallest x position. The error bars are +/- 31 nm, and stem from the resolution of the images causing an uncertainty of +/- 22 nm when recording the pixel position of a sample edge or a vortex core center. Determining a vortex core position requires two pixel positions: that of an edge and a core center. Error propagation gives a total vortex core position uncertainty of +/- 31 nm.

Recalling the ellipticity of the theoretical trajectories shown in Figure 3.6, and noting that this experiment is measuring trajectories much closer to resonance than those depicted, it becomes apparent that the deviation off of a perfect circular trajectory would be quite minimal. K.-S. Lee has calculated that for $\omega_H/\omega_D = 0.9$ and 1.1, an ellipticity of about 0.43 can be expected[71]. This is a very challenging ellipticity to observe with the current experimental capabilities. For example, if the trajectory exactly at resonance had a radius of 70 nm, an ellipticity of 0.43 would correspond to an ellipse with radii of 72 nm and 65 nm. Detecting the elongation of the trajectories would require measurement error under 10 nm.

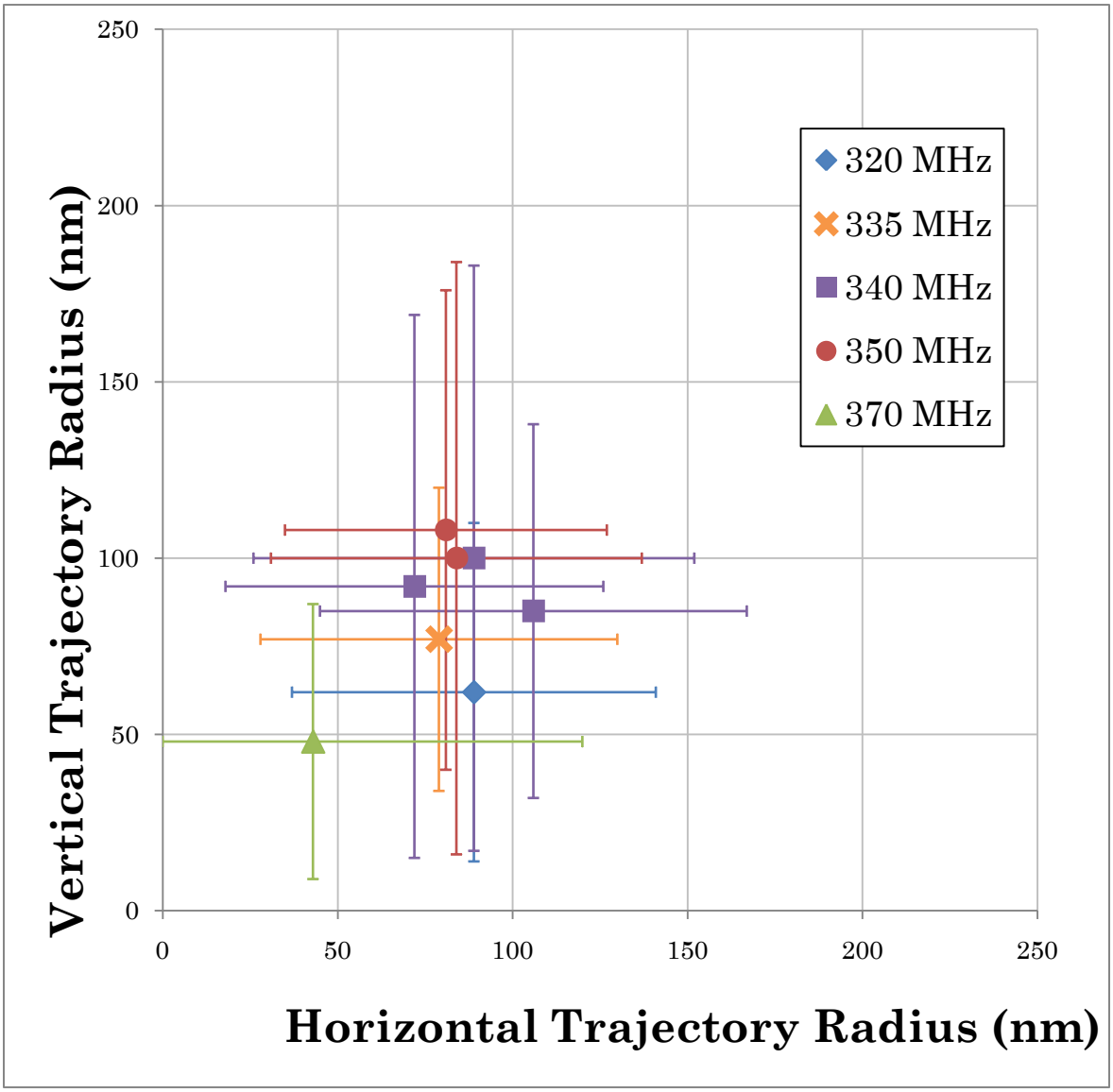

Figure 3.9 Vortex core trajectory radii for a number of driving frequencies and an amplitude of 4 Oe.

A significant portion of the error introduced is caused by the resolution of the images and the uncertainty of picking the pixel that is the sample edge or core. This could be mitigated by examining line profiles of the image and fitting step functions to the edges and Gaussians to the

core, resulting in some error from fitting, but much less than the +/- 22 nm from the current technique. Such an approach was not justifiable with the present data due to inconsistent and non ideal image quality. Images were often sufficiently noisy such that the core could not be distinguished from the line profile alone. In addition, the exact position of the edge is difficult to pinpoint for a few reasons. First, the partial coherence of the bending magnet radiation can cause interference effects which distort the edges of the sample in the image. Second, the images being examined are difference images and require the alignment and division of two component images where the alignment is often imperfect as discussed further below. The combination of the edge distortion from the coherence, and the slight alignment imperfections results in line profiles where the edges of the sample are spread out and not simple step functions.

The issue of noisy images is partly due to the nature of these time-resolved experiments where the photon flux is so low and where for these samples the x-rays had to pass through 100 nm of Au before reaching the CCD. (The photon intensity at the sample is roughly 10 times less in two-bunch mode than in the normal ALS operational mode.) Longer image exposure times can help; however, in this experiment images already took 10 minutes to record, 20 minutes for a set of two images with opposite contrast. Increasing the exposure times would not only limit the number of images taken in an experiment, but beyond a certain point would not improve image quality as longer images require long term stability of the microscope and the illumination. As mentioned above, the imperfect alignment of the difference images, which muddies the imaging of the sample edges, is due to the method of selecting photons with opposite polarizations. X-rays of opposite polarities are chosen by selecting a higher or lower portion of the incoming light, but the optics themselves cannot be moved with the current configuration of the microscope. This can cause dramatic differences in the spatial location of the sample in the image view and even differences in the strength of the magnetic contrast. In addition, the image quality typically drifts over time as the direction of light from the synchrotron changes or microscope components drift or degrade. Thus for a large survey such as was done here, a consistent image quality is challenging to achieve.

Soft x-ray microscopy is currently a powerful tool for magnetic studies and has the potential to be developed further to enable more challenging investigations, like that of the detailed vortex core trajectory analysis attempted here. Issues such as equipment drift are an engineering challenge and are constantly being addressed and improved at XM-1. Spatial resolution is a fabrication and an engineering challenge and is also under continuous improvement[45,72-74]. A soft x-ray microscope using fully controllable elliptically polarized light from an undulator will solve many of the magnetic contrast and image alignment concerns. With an x-ray source that could be tuned to provide opposite helicities of light, instead of an x-ray source where the helicities must be selected spatially, alignment issues between images with opposite contrast should be mitigated and magnetic contrast should be easier to predict and maintain. However, the issue of distortion of the sample edges could be exacerbated with the use of undulator radiation which is more coherent than bending magnet radiation. If an x-ray microscope was designed to be illuminated with elliptically polarized undulator radiation, special attention would have to be given to the degree of coherence of the photons arriving at the sample. The problem of limited photon flux available for time-resolved experiments is tied to current x-ray sources. Future fsec soft x-ray sources operating near the Fe, Ni, and Co edges with high photon flux in nominally 20 fsec pulses will offer the opportunity for single shot images of magnetic dynamics[75]. Beyond studying vortex core displacements, x-ray sources with

fsec resolution will enable studies of other magnetic dynamics such as the exact process of vortex core polarity flipping.

3.3 Summary of Resonant Vortex Core Motion Studies

The studies described here of the magnetization dynamics in a 2 μm diameter $Fe_{20}Ni_{80}$ cylinder with a thickness of 100 nm are early steps towards a detailed understanding of vortex core dynamics. Using a non time-resolved technique an interesting nonlinear response of the vortex core was observed. Time-resolved images using a phase-locking technique confirmed the reliability of the non time-resolved approach. The resonance frequency determined using non time-resolved imaging was shown to correspond to a driving frequency for gyrotropic motion in the time-resolved imaging experiment. The ability to gain useful information about magnetization dynamics without needing the more time intensive time-resolved images is invaluable. Future studies of vortex cores can be run first without time resolution to quickly determine areas of dynamics, and then interesting conditions, such as specific driving frequencies, can be reproduced and the core response to these conditions can be imaged with time resolution. The evidence of modesplitting observed which was observed experimentally needs further theoretical support. A time-resolved experiment probing this effect would be interesting.

An attempt to observe the details of vortex core trajectories in the linear regime was also described here. Unfortunately, the spatial resolution of current x-ray microscopy is not sufficient to resolve such details. Future development of x-ray transmission microscopy will enable such studies, and others involving ultrafast spin dynamics.

Chapter 4 Spin Dynamics: Vortex-antivortex Dynamics

The dynamic response of spins in patterned magnetic materials is an area of particular interest in the scientific and technological communities[76-80]. This chapter details a study of the dynamic response of the magnetization in a rectangular $Fe_{20}Ni_{80}$ structure. Time-resolved images reveal that after the application of a fast field pulse, the two magnetic vortex cores in the structure deform and a stripe domain is briefly formed between the cores. Upon comparison with micromagnetic simulation, the stripe domain is shown to be evidence of vortex-antivortex core pair formation. This experimental demonstration of vortex-antivortex pair creation during vortex excitation lends strong support to theories which suggest that a vortex-antivortex core pair is formed when the polarity of a vortex core is switched.

Beyond the single vortex in circular disks, which was investigated in the previous chapter, patterned magnetic elements can display other interesting, and repeatable, spin configurations[11,16]. The sample studied in this chapter, a 2 μm x 4 μm x 45 nm $Fe_{20}Ni_{80}$ rectangle, displays a 7-domain Landau flux closure state at remanence (Fig 4.1 (a)). Using a pump-probe experimental technique, x-ray transmission microscopy images of the in-plane magnetic configuration were taken in 100 ps steps following an excitation of the system from a magnetic pulse with a 100 ps rise time. As indicated in Figure 4.1, the spin dynamics observed included a stripe domain forming across the center domain and a deformation of the vortex cores. Upon further investigation of the images, the dynamic response was shown to depend on the initial polarity of the vortex cores. In addition, comparing these results to micromagnetic simulations run by K. J. Lee[81] revealed that the observed changes in the magnetic domain configuration indicate the presence of magnetic vortex-antivortex core pairs.

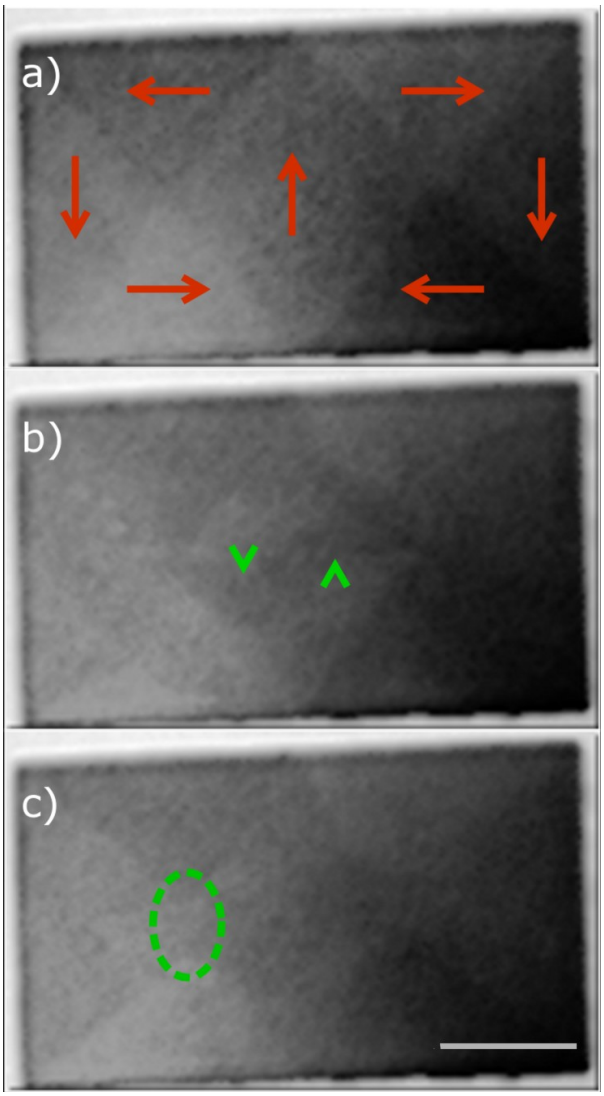

Figure 4.1 Representative sequence of normalized images of a 2 x 4μm^2 $Fe_{20}Ni_{80}$ element. The external field direction to saturate the sample is along the long axis, while the exciting magnetic field pulse is along the short axis of the rectangular element. Scale bar is 1μm. (a) Ground state configuration of the rectangular patterned $Fe_{20}Ni_{80}$ element. The red arrows indicate the direction of in-plane magnetization. The tilt of the sample was along the short axis; therefore, the three center domains do not show magnetic contrast in the x-ray image. (b) Image taken after 1ns. The green brackets highlight a dark contrast stripe domain across the center domain. (c) Image taken after 1.6ns. The deformed vortex core area is circled.

While the antivortex is seen paired with the vortex in static magnetic structures such as cross tie walls[21-23,82-83], magnetization dynamics involving vortex-antivortex core pairs are distinctly important. In particular, vortex-antivortex core pairs are predicted by theory to play a central role in the dynamics of switching a vortex core polarity. A complete understanding of the magnetization configuration throughout the course of a vortex core polarity flip would be valuable in developing future technologies where the binary nature of the polarity of the core could be used for information storage. Vortex core polarity switching has been observed repeatedly in experiments[4,28], however the process of switching has not been recorded. A

prominent feature of the switching models developed is the creation and annihilation of a vortex-antivortex core pair during switching[4,26,61,83-86]; however, very little clear experimental evidence of this has been shown. In Figure 4.2, a proposed switching mechanism by Waeyenberge et al. is outlined[4]. Experimentally, the study of vortex-antivortex core pairs is challenging because of their short lifetimes, on the order 10 ps[83-84], as well as their size, on the order of 10 nm[77]. In this chapter, evidence of vortex-antivortex core pairs during the excitation of vortices is demonstrated. This gives further support to the idea that vortex-antivortex core pairs are an integral part of vortex core dynamics.

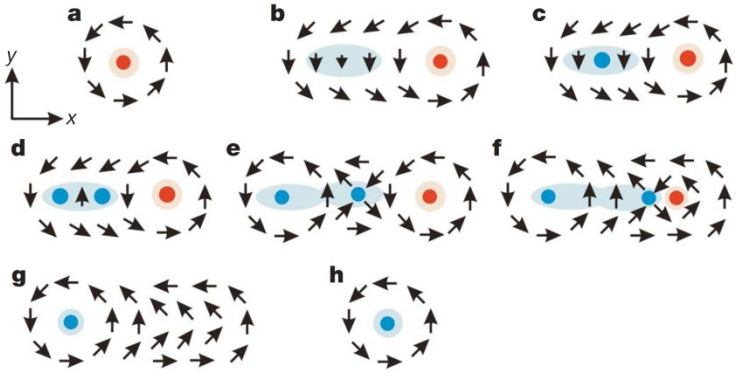

Figure 4.2 This figure illustrates the proposed switching mechanism of Waeyenberge et al. where the vortex-antivortex pair is seen in steps e) and f). Black arrows represent in-plane magnetization components and the red and blue dots represent in- and out-of-plane magnetization respectively. Figure from [4].

4.2 Observations of Spin Dynamics in a Permalloy Rectangle

The time resolved experiments described here were performed at XM-1 during the 2-bunch mode operation of the ALS using the pump probe experimental technique described in section 2.6.1and images were taken using 854eV (1.45nm) radiation, which corresponds to the nickel L_3 edge. The time resolution was 70 ps. For this experiment the sample was tilted at a 60 degree angle compared to the incident photons to allow the in-plane magnetic components to be imaged (Fig. 2.5(b)). Before a sequence of images was taken, the sample was saturated with an external field of 1 kOe along the long axis of the rectangle. As can be seen in Figure 4.4 the field is applied in the plane of the sample with a slight out-of-plane component. Images of the saturated sample can then be used to normalize the sequence of images following the magnetization dynamics.

Figure 4.1 illustrates some prominent features of the magnetization dynamics which were imaged; a stripe domain temporarily forms across the middle domain, and a deformation of the magnetization in the vortex core regions occurs. A more complete sequence of images is shown in Figure 4.3. Here the images were smoothed over several pixels and normalized with an image of the sample with saturated magnetization to emphasis the evolution of the domains; difference images are placed to the right of each image to further underline the prominent features of each stage of dynamics. The vortex cores move over the course of the dynamics; for example, at 1000 ps after time zero it is clear that the vortices have shifted inwards. Also around this time delay, one can observe that as the central domain shrinks, the domains parallel to the perturbing field pulse have expanded, with the domain wall now bulging outward. The inward motion of the

vortex cores towards each other is a distinct departure from the simple gyrotropic motion seen in Chapter 3 and other studies where only one vortex structure is present[4-5,28,69].

The stripe domain appears at 400 ps after time zero and remains visible until 1400 ps, giving it a lifetime of about 1 ns. The domain did not appear again in a full 8 ns scan of time, indicating that the stripe only exists during the initial excitation of the magnetization. A possible consideration is that this feature is the result of an excited spin wave mode. Using the 1 ns lifetime of the pattern as a half-wave period, this would correspond to a ~ 0.5GHz spin wave mode. This would be too slow for this geometry where a frequency of several GHz is expected[87].

While the stripe domain seen in Figure 4.3 has dark contrast and stretches diagonally across the center domain from the lower left to the upper right, other sequences of images show the stripe domain with the opposite contrast and spatial configuration (Fig. 4.4). Upon further investigation, the magnetization of the domain, and the spatial orientation, can be related to the initial saturation of the sample. Prior to taking a sequence of images at varying time delays, the sample was saturated with an external field, the direction of which was varied over the course of the experiment. As is depicted in Figure 4.4, the configuration of the experiment meant that a small component of the external field was normal to the plane of the sample, so that depending on whether the saturated field was applied in-plane to the right or left, there was a small external field applied into or out of the plane of the sample. This out-of-plane component of the saturating field was an experimental artifact; however, it produced interesting results. The light stripe domain was seen when the saturating field had a component pointing up out of the plane while the dark was seen when there was a component pointing down into the plane. It should be emphasized that the in-plane magnetization structure of the six configurations shown in Figure 4.4 are all alike, each displaying the 7-domain Landau flux closure structure with the same sense of rotation of the magnetization around the vortex cores. Thus, the out of plane portion of the magnetization, the polarity of the vortex cores, is the only initial configuration difference. The polarity of the vortex cores seems to have been aligned to the normal component of the saturating field. This in turn determined the dynamic response of the in-plane magnetization. It has been demonstrated previously that the core polarity determines the gyrotropic motion of the vortex core[5]. The results presented here show that the polarity of the core can influence the dynamics of the structure even during nongyrotropic motion. Interestingly, in this case with two vortex cores, the sense of the motion itself remains the same, always inward; however, the in-plane magnetization is still affected by the core polarity.

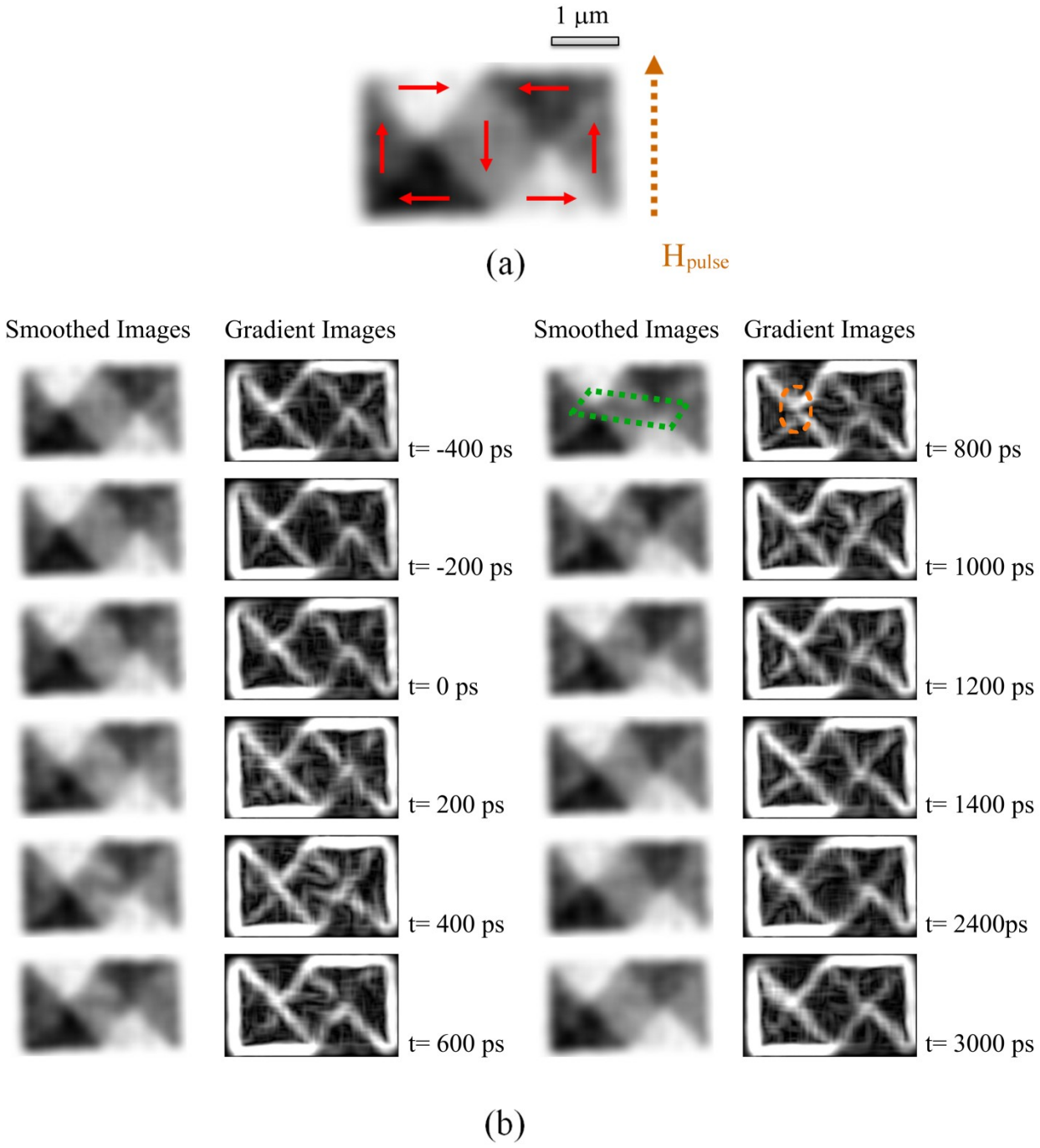

Figure 4.3 Typical sequence of soft x-ray images. (a) The remanent state is shown here with the red arrows indicating the in-plane magnetization. The brown dotted arrow indicates the direction of the perturbing field pulse. This image has been smoothed over several pixels and normalized with an image of the sample with saturated magnetization. (b) Smoothed and normalized images for various time delays are shown with the corresponding gradient images to the right. Field pulse is switched on at t=0ps. At t= 800 ps two features are emphasized. The dotted green box highlights the dark stripe domain and the dotted orange circle highlights the distorted vortex area. These features are seen with varying clarity at several time delays. Figure from [81].

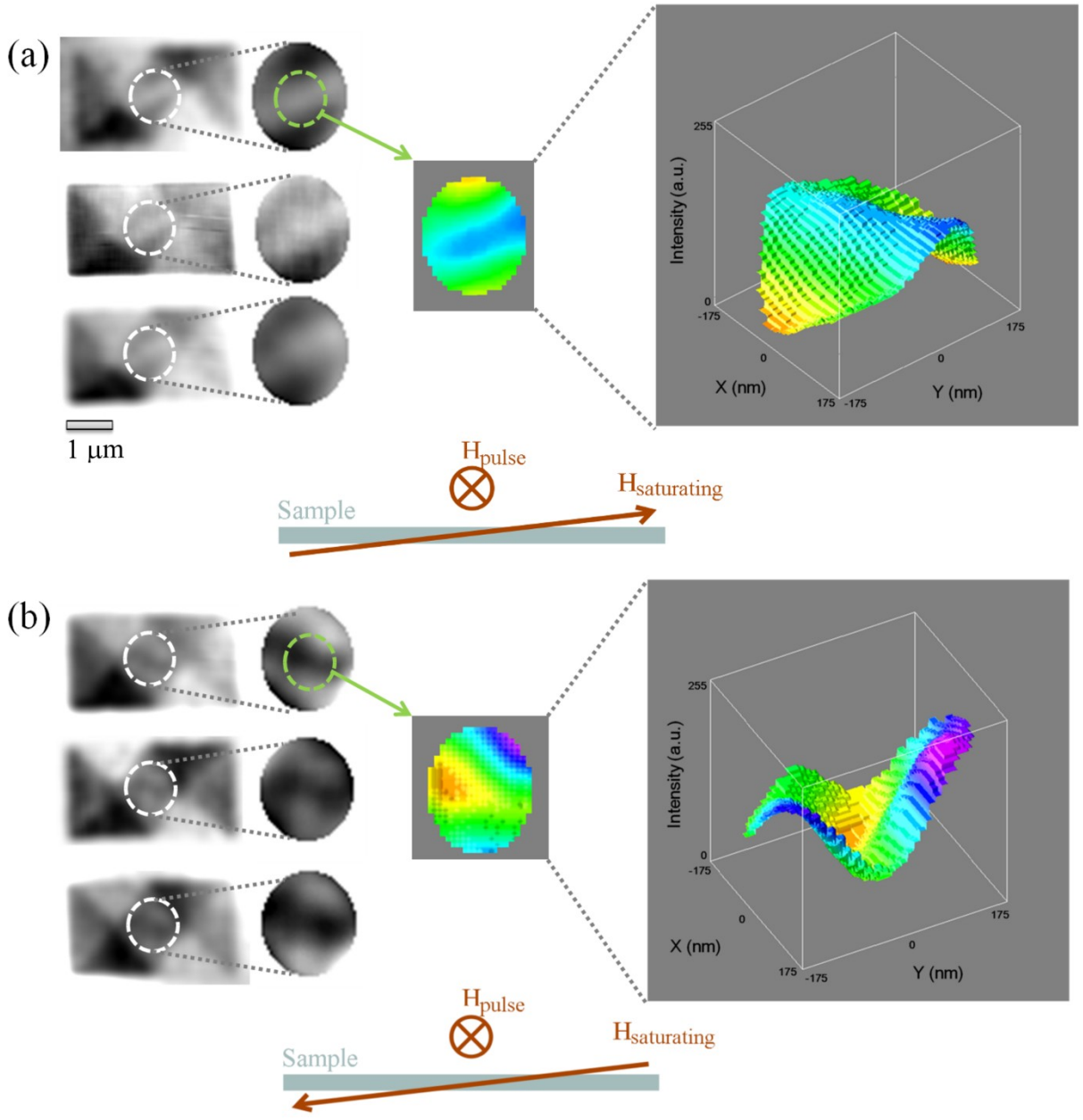

Figure 4.4 Contrast of the stripe domain compared to saturating field. Images are taken at an 800 ps time delay. Several examples of the stripe domains are shown. To emphasize the contrast of the domain, intensity plots of the image are shown for representative images. In (a) several examples of a stripe domain with light contrast stretching from the lower left to the upper right are shown. For each of these examples the initial saturating field was slightly out of the plane of the sample. In (b) several examples of a stripe domain with dark contrast stretching from the upper left to the lower right are shown. For each of these examples the initial saturating field was slightly into the plane of the sample. Figure from [81].

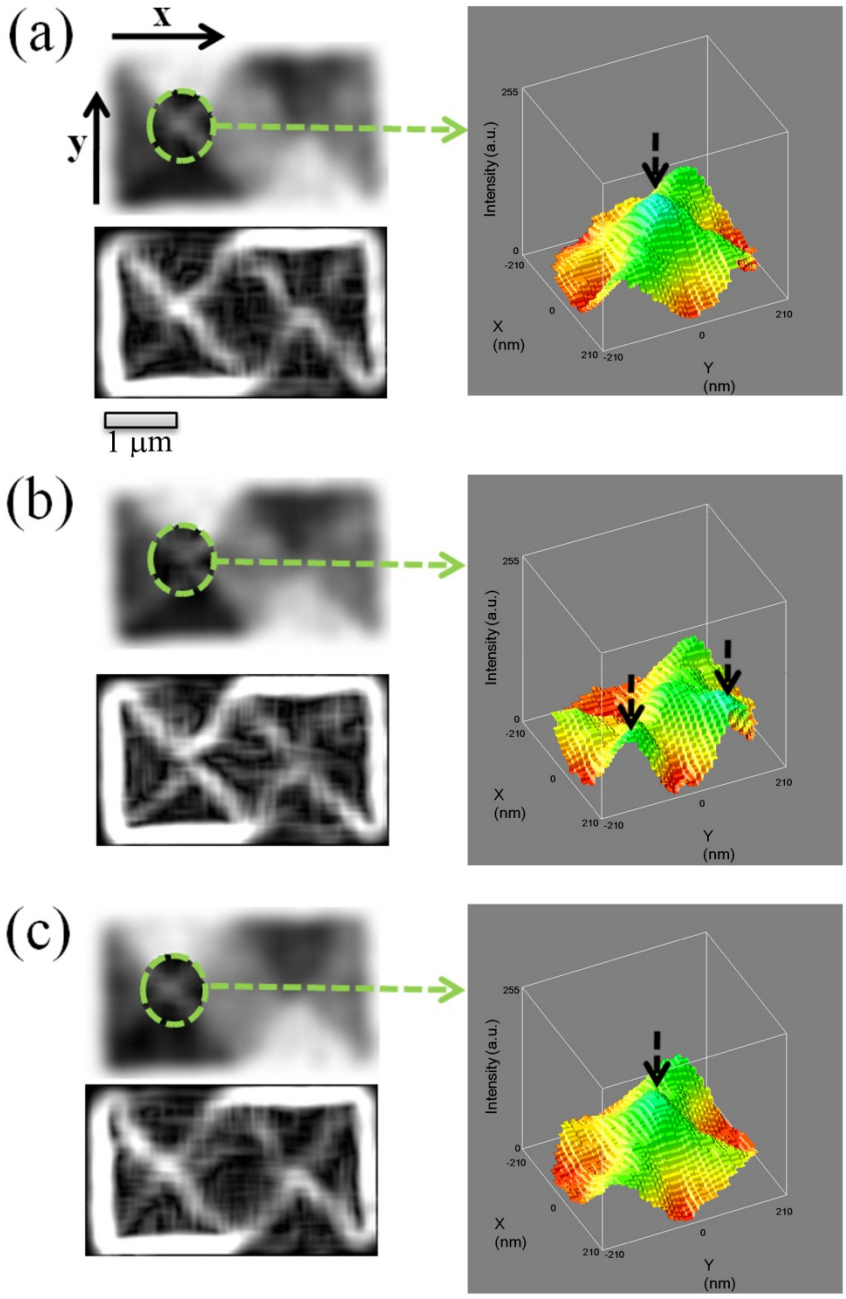

Figure 4.5 Sequence of images highlighting the deformation of the vortex core. (a) The sample after 0 ps delay, (b) 800 ps delay, and (c) 2400 ps delay. The smoothed and normalized images at each time delay are shown with the corresponding gradient images as well as an intensity plot of the vortex core region. Black arrows on the intensity plot point out peaks. The single peak seen in (a) has become two peaks in (b), and returns to one peak in (c). Figure from [81].

There is one additional key feature of the magnetization dynamics, the deformation of the vortex cores. In Figure 4.3, the deformation of the left vortex core area is discernable in the gradient image at 800 ps delay where there is a clear split of the vortex core compared to images at earlier time delays. This can be examined more completely in Figure 4.5 where the intensity

profile of the image, which peaks at the vortex core, changes drastically at 800 ps delay. At this delay there are two peaks in the intensity plot separated along the y axis. The intensity profile returns to a single peak after several nanoseconds. It is clear now why the core motion is nongyrotropic; the vortex core is not behaving as a rigid object, as is assumed in models predicting gyrotropic motion[57,60-61]. In future studies, a higher spatial resolution, closer to 10 nm, could facilitate imaging of the exact nature of the core deformation. For the purposes of this study, the details of the deformation of the vortex cores were further explored through micromagnetic simulations.

4.3 Simulations of Spin Dynamics in a Permalloy Rectangle

Micromagnetic simulations run by K. J. Lee[81] provided a more detailed understanding of the dynamics occurring in this experiment. In general, micromagnetic simulations start with a mesh where each cell in the mesh is assigned a 3-D magnetization vector. The magnetization dynamics for each cell are then calculated using any specified magnetic properties, the magnetization from neighboring cells, and any external fields or currents. The simulations for this experiment were run using a code which solves the Landau-Lifshitz-Gilbert equation using the 4th-order Runge-Kutta method[81,88-89], where the Landau-Lifshitz-Gilbert equation defines the change in magnetization as follows[11,13]:

$$\frac{d\vec{M}}{dt} = -\gamma\left[\vec{M} \times H_{eff}\right] + \frac{\alpha}{\left|\vec{M}\right|}\left[\vec{M} \times \frac{d\vec{M}}{dt}\right] \tag{4.1}$$

The first term accounts for the precessional motion of the magnetization in an effective local magnetic field, H_{eff}, that combines the affect of the relevant energies on the magnetization vector; γ is the gyromagnetic ratio. The second term describes the damping of the magnetization and the relaxation into the direction of the resulting effective magnetic field; α is a phenomenological parameter describing this relaxation, which depends on the anisotropy, the geometry, and the morphology of the specimen. The relevant vectors seen in the Landau-Lifshitz-Gilbert equation are shown in Figure 4.6.

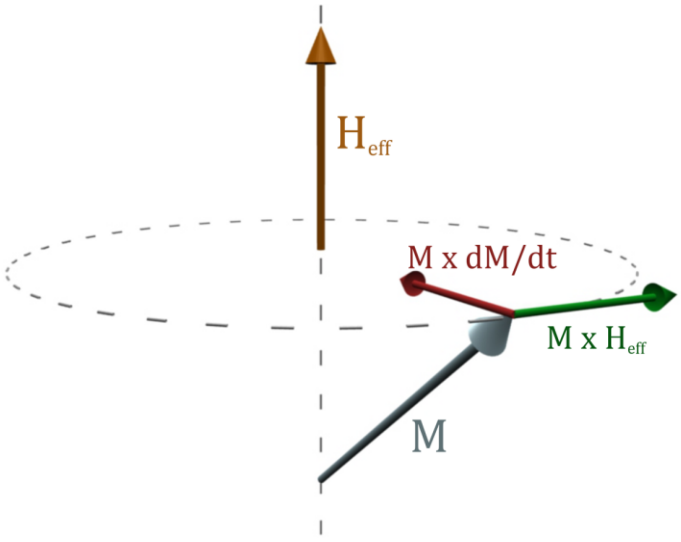

Figure 4.6 Magnetization dynamics as described by the Landau-Lifshitz-Gilbert equation.

For the simulations described here, a rectangular mesh with the same areal dimensions as the physical sample and a cell size of 5 x 5 x 10 nm^3 was used; α was set to 0.01[81]. The initial state of the sample was set to a 7-domain Landau pattern and the dynamics were examined after a 1 ns pulse with field strength of 100 Oe was applied. Two cases were investigated, positive and negative core polarity (p=+1 and p=-1).

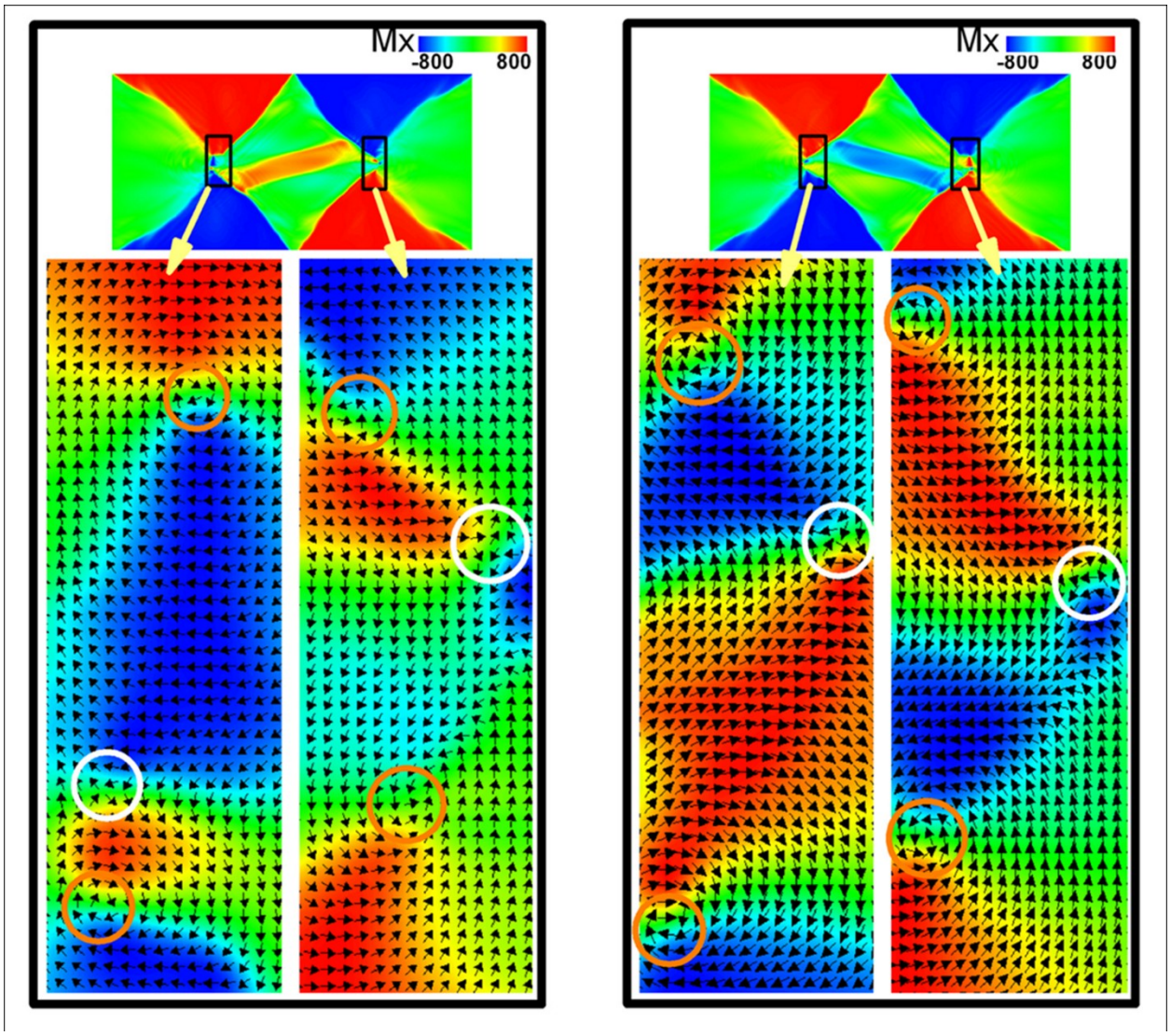

Figure 4.7 Images from simulation showing magnetization 800 ps after field pulse. The case of p=+1 is shown on the right and the case of p=-1 is shown on the left. The full samples are shown with enlargements of the vortex core areas below. As in experimental images, the magnetization direction along one axis is shown; where red indicates magnetization pointed fully to the right, and blue fully to the left. Vortex cores are highlighted with orange circles, and antivortex cores with white circles. Figure from [81].

Comparing the larger features of the magnetization, a good match is found between experiment and simulation. The inward trajectories of the vortex cores is seen for both cases of core polarity, as are the bulging walls that increase the size of domains magnetized in the direction of the field pulse. As can be seen in Figure 4.7, the stripe domain is also observed to

form in the simulations. The images from simulation seen in Figure 4.7 show the magnetization 800 ps after the application of the pulse, and thus can be directly compared to the images from experiment shown in Figure 4.4. The domain shape and magnetization observed in experiment has been reproduced in the simulations. In addition, the lifetime of the stripe domain matches that seen in experiment.

The nanoscale 5 x 5 nm^2 areal cell size used in these simulations allows smaller features of the magnetization, not resolvable in the current experiments, to be scrutinized. The deformation of the vortex core area at 800 ps, seen as an indistinct splitting of the core in experiment, can now be confirmed. There is a clear stretching of the vortex core area along the y-axis. Also, as shown in Figure 4.7, a vortex-antivortex core pair has been generated. The pair appears to stay at the domain wall region. This position costs less exchange energy and thus temporarily stabilizes the pair. The exchange energy is relieved over the central domain, with the stripe domain growing from each of the vortex-antivortex core pairs, finally connecting the pairs together and forming the full stripe domain. We see this behavior for both p=+ and p=-1 where, as observed for the stripe domain in the experiment, the geometry and magnetization direction in one case are opposite to the other (Fig 4.8).

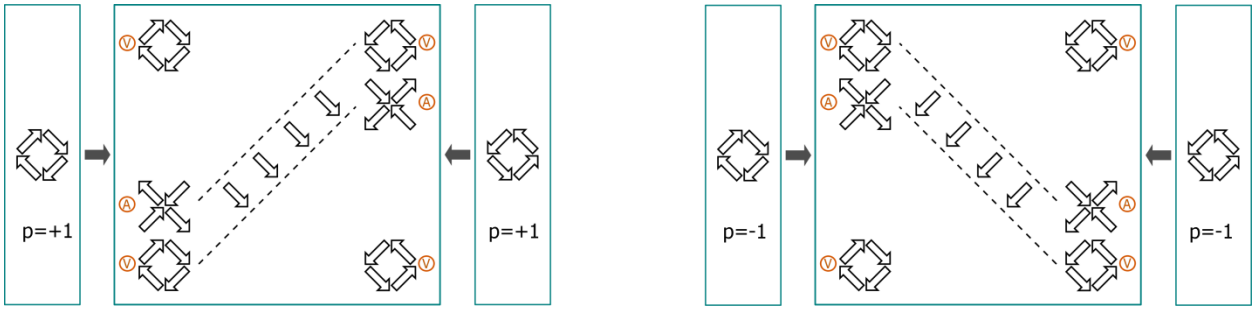

Figure 4.8 Schematic depictions of the initial vortex core configurations and the resulting configurations 800 ps after the perturbing field pulse was applied. Figure following [81].

While the details of the dynamics in the core area could not be imaged in experiment, it should be emphasized that the experimental findings could be reproduced with this simulation. In particular, the shape, contrast, and timescale of the stripe domain have been reproduced. As learned from the simulations, the stripe domain is a result of the interaction between the vortex-antivortex core pairs; the image of the stripe domain in experiment shows indirect proof of this interaction. The experiment thus provides an indication of the existence of the vortex-antivortex core pairs.

4.4 Summary of Spin Dynamics in a Permalloy Rectangle

The study described here of a 2 µm x 4 µm x 45 nm $Fe_{20}Ni_{80}$ rectangular sample provides interesting insight into the dynamic response of vortex cores. Using a pump and probe technique, images were taken as the 7-domain Landau flux closure domain configuration dynamically responded to a short field pulse. The vortex cores exhibited nongyrotropic motion, moving symmetrically inwards towards one another. Simulations revealed that the vortex core area deformed, and a vortex-antivortex core pair was generated at each vortex core site, resulting in a connecting stripe domain forming across the central domain.

Interestingly, the vortex-antivortex core pairs did not play a role in switching the core polarity. Because the pump and probe experimental setup only allows imaging of magnetization dynamics that are reproducible for each pump and probe cycle, and the polarity of the cores determines the geometry and contrast of the stripe domain, the polarities could not have flipped during the repeated excitations.

While core switching did not occur in this experiment, the findings do provide indirect but significant evidence that a vortex-antivortex core pair is generated when a vortex core is excited, as has been predicted in the switching models. This is important to furthering our understanding of the dynamics of the vortex core, especially in light of potential future applications.

Chapter 5 Conclusion

This dissertation addressed the study of nanoscale spin dynamics in confined geometries using soft x-ray transmission microscopy. Specifically, the dynamic response of magnetic vortex cores to external fields was studied using a variety of soft x-ray transmission microscopy techniques. Specialized samples designed for these studies were fabricated onto waveguides through which current could be driven to create magnetic fields in the plane of patterned magnetic elements. The samples consisted of Si_3N_4 membrane substrates with Au waveguides and patterned $Fe_{20}Ni_{80}$ elements.

Chapter 3 described studies on the resonant vortex core motion in a thin circular $Fe_{20}Ni_{80}$ pattern which had a diameter of 2 μm and a thickness of 100 nm. The resonant vortex core motion in this disk was first studied using time-averaged, or non time-resolved, imaging. A technique was developed to use this type of imaging to determine significant information about the dynamic behavior of the vortex core. The vortex core was imaged as oscillating driving fields were applied with a range of RF frequencies and amplitudes. The image of the core remained clear for most frequencies, but when specific driving frequencies and amplitudes were applied, the image of the core blurred or disappeared, suggesting dynamic motion was occurring as a response to a resonant frequency. This was a reproducible and repeatable effect, and the reliability of this technique was later confirmed with time-resolved images. The study using non time-resolved imaging revealed an unexpected nonlinear response of the vortex core which will require further experiments and theory to understand fully.

Using the same thin circular sample, and using a phase-locking technique to obtain time-resolved images, Chapter 3 also described preliminary work done to investigate the trajectory of a vortex core when excited by RF fields with frequencies on either side of the resonant frequency. The vortex core motion was imaged with a 70 ps time resolution. However, a full survey of the vortex trajectories at frequencies surrounding the resonance frequency was not possible as the spatial resolution of current x-ray microscopy was not sufficient to resolve small deviations, on the order of 10 nm, in the vortex core trajectories. This experiment tested the present limits of soft x-ray transmission microscopy. Future development of x-ray transmission microscopy will enable such studies, and others involving ultrafast spin dynamics. With the current configuration of the soft x-ray transmission microscope, XM-1, several improvements can be made such as increased spatial resolution and the minimization of the drift of microscope

components over time. These are already areas of continual improvement at XM-1. A more radical and far-reaching improvement would be to illuminate the microscope with elliptically polarizing undulator radiation rather than with bending magnet radiation. This would give users consistent control over the polarization of the illuminating radiation without shifting the image on the CCD, thus facilitating easy alignment for difference images. However, use of undulator radiation would require special attention to the degree of coherence of the illumination.

In Chapter 4, spin dynamics were investigated in a thin rectangular $Fe_{20}Ni_{80}$ pattern which had areal dimensions of 2 μm x 4 μm and a thickness of 100 nm. The response of the magnetization to a fast magnetic field pulse was imaged using a pump-probe time-resolved technique. Vortex cores in the initial magnetization configuration were excited and deformed, and a stripe domain formed across the center domain, after the application of the field pulse. Comparison with simulation gives strong evidence that vortex-antivortex core pairs were created and annihilated during the vortex core excitation. Vortex-antivortex core pairs frequently appear in theoretical calculations of vortex core polarity switching. The experiment described in Chapter 4 provides strong support for these models. To follow the exact dynamic process of vortex-antivortex creation and annihilation, improved spatial and temporal resolution is needed. Future fsec soft x-ray free electron lasers offer the opportunity for microscopes with increased temporal resolution, opening this field to many new spin dynamics studies on a fsec timescale.

A deeper understanding of the dynamic response of the vortex core is essential to lead the way to future technological applications which could take advantage of the multiple vortex core configurations to store more information in a smaller device. In general, the expanding field of spintronics offers many exciting possibilities for future technologies. Improved analytical tools are necessary to broaden our understanding of spin dynamics. Magnetic soft x-ray imaging is an indispensable and powerful tool for magnetic studies and has to be developed further to enable ever more challenging investigations.

References

1. H. Zheng, J. Wang, S. E. Lofland, Z. Ma, L. Mohaddes-Ardabili,T. Zhao,L. Salamanca-Riba,S. R. Shinde,S. B. Ogale,F. Bai,D. Viehland,Y. Jia,D. G. Schlom,M. Wuttig, A. Roytburd,R. Ramesh, *Science* **303**, 661 (2004).

2. J. M. D. Coey, M. Venkatsan, and C. B. Fitzgerald, *Nature* **4,** 173 (2005).

3. W. Eerenstein, N. D. Mathur, and J. F. Scott, *Nature* **442,** 759 (2006).

4. B. Van Waeyenberge, A. Puzic, H. Stoll, K. W. Chou, T. Tyliszczak, R. Hertel, M. Fähnle, H. Bruckl, K. Rott, G. Reiss, I Neudecker, D. Weiss, C. H. Back, and G. Schutz, *Nature* **444**, 461 (2006).

5. S.-B. Choe, Y. Acremann, A. Scholl, A. Bauer, A. Doran, J. Stöhr, and H. A. Padmore, *Science* **304**, 420 (2004).

6. S.-H. Jun, J.-H. Shim, S.-K. Oh, S.-C. Yu, D.-H. Kim, B. Mesler, and P. Fischer, *Appl. Phys. Lett.* **95**, 142509 (2009).

7. J.-H. Shim, D.-H. Kim, B. Mesler, J.-H. Moon, K.-J. Lee, E. Anderson, and P. Fischer, *J. Appl. Phys.*. **107**, 09D302 (2010).

8. M. Yamanouchi, D. Chiba, F. Matsukura and H. Ohno, *Nature* **428**, 539 (2004).

9. Luc Thomas, Masamitsu Hayashi, Xin Jiang, Rai Moriya, Charles Rettner & Stuart S. P. Parkin, *Nature* **443**, 197 (2006).

10. S. D. Bader, S. S. P. Parkin, *Annu. Rev. Condens. Matter Phys.***1**, 3 (2010).

11. A. Hubert, and R. Schäfer, Magnetic Domains: The Analysis of Magnetic Microstructures, (Springer, New York, 2000).

12. D. Goll, G. Schütz, and H. Kronmüller, *Phys. Rev. B* **67**, 094414 (2003).

13. J. Stohr, H. C. Siegmann, Magnetism: From Fundamentals to Nanoscale Dynamics, (Springer, Berlin, Heidelberg, New York, 2006).

14. N. Spaldin, Magnetic Materials: Fundamentals and Device Applications, (Cambridge University Press, Cambridge, 2003).

15. D. O. Smith, *J. Appl. Phys.* **30**, S264 (1959).

16. P. Fischer, G. Denbeaux, T. Ono, T. Okuno, T. Eimüller, D. Goll, and G. Schütz, *J. Phys. D: Appl. Phys.* **35,** 2391 (2002).

17. T. Shinjo, T. Okuno, R. Hassdorf, K. Shigeto, and T. Ono, *Science* **289**, 930 (2000).

18. A. Wachowiak, J. Wiebe, M. Bode, O. Pietzsch, M. Morgenstern, and R. Wiesendanger, *Science* 298, **577** (2002).

19. W. Scholz, K. Yu. Guslienko, V. Novosad, D. Suess, T. Schrefl, R. W. Chantrell, and J. Fidler, *J. Magn. Magn. Mater.* **266**,155 (2003).

20. A. Drews, B. Kruger, M. Bolte, and G. Meier, *Phys. Rev. B* **77**, 094413 (2008).

21. K. Shigeto, T. Okuno, K. Mibu, T. Shinjo, and T. Ono, *Appl. Phys. Lett*. **80**, 4190 (2002).

22. E. E. Huber, Jr., D. O. Smith, and J. B. Goodenough, *J. Appl. Phys*. **29**, 294 (1958).

23. S. Middelhoek , *J. Appl. Phys*. **34**, 1054 (1963).

24. R. P. Cowburn, *Nature Mater.* **6**, 255 (2007).

25. N. Kikuchi, S. Okamoto, O. Kitakami, Y. Shimada, S. G. Kim, Y. Otani, and K. Fukamichi, *J. Appl. Phys.* **90**, 6548 (2001).

26. S.-K. Kim, Y.-S. Choi, K.-S. Lee, K. Y. Guslienko, and D.-E. Jeong, *Appl. Phys. Lett.* **91**, 082506 (2007).

27. S.-K. Kim, K.-S. Lee, Y.-S. Yu, and Y.-S. Choi, *Appl. Phys. Lett.* **92**, 022509 (2008).

28. K. Yamada, S. Kasai, Y. Nakatani, K. Kobayashi, H. Kohno, A. Thiaville, and T. Ono, *Nature Mater.* **6**, 269 (2007).

29. H.-G. Piao, D. Djuhana, S.-K. Oh, S.-C. Yu, and D.-H. Kim, *Appl. Phys. Lett.* **94**, 052501 (2009).

30. I. Tudosa, C. Stamm, A. B. Kashuba, F. King, H. C. Siegmann, J. Stöhr, G. Ju, B. Lu, and D. Weller *Nature* **428**, 831 (2004).

31. C. D. Stanciu, F. Hansteen, A.V. Kimel, A. Kirilyuk, A. Tsukamoto, A. Itoh, and Th. Rasing, *Phys. Rev. Lett.* **99**, 047601 (2007).

32. C. H. Back, R. Allenspach, W. Weber, S. S. P. Parkin, D. Weller, E. L. Garwin, H. C. Siegmann, *Science* **285**, 864 (1999).

33. Th. Gerrits, H. A. M. van den Berg, J. Hohlfeld, L. Bär, and Th. Rasing *Nature* **418** 509 (2002).

34. K. Vahaplar, A. M. Kalashnikova, A.V. Kimel, D. Hinzke, U. Nowak, R. Chantrell, A. Tsukamoto, A. Itoh, A. Kirilyuk, and Th. Rasing, *Phys. Rev. Lett.* **103**, 117201 (2009).

35. E. B. Myers, D. C. Ralph, J. A. Katine, R. N. Louie, R. A. Buhrman, *Science* **285**, 867 (1999).

36. S. S. P. Parkin, M. Hayashi, L. Thomas, *Science* **320**, 190 (2008).

37. L. Bocklage, B. Kruger, R. Eiselt, M. Bolte, P. Fischer, G. Meier, *Phys. Rev. B* **78**, 180405 (2008).

38. G. Meier, M. Bolte, R. Eiselt, B. Kruger, D.-H. Kim, P. Fischer, *Phys. Rev. Lett.* **98**, 187202 (2007).

39. D. Attwood, Soft X-rays and Extreme Ultraviolet Radiation: Principles and Applications, (Cambridge University Press, New York, 1999)

40. P. Fischer, D. H. Kim, B. L. Mesler, W. Chao, A. Sakdinawat, and E. H. Anderson, *Surf. Sci.* **601** 4680 (2007).

41. P. Fischer, D. H. Kim, B. L. Mesler, W. Chao, and E. H. Anderson, *J. Magn Magn. Mater.* **310** 2689 (2007).

42. C. T. Chen, F. Sette, Y. Ma, and S. Modesti, *Phys. Rev. B* **42**, 7262 (1990).

43. P. Fischer, D.-H. Kim, W. Chao, J. A. Liddle, E. H. Anderson, and D. T. Attwood, *Materials Today* **9**, 26 (2006).

44. B. L. Mesler, K. Buchanan, M.-Y. Im, E. Anderson, and P. Fischer *J. Vac. Sci. Technol. B* **28**, 198 (2010).

45. W. Chao, M.-Y. Im, S.B. Rekawa, E. Anderson, P. Fischer to be published (2010).

46. U. Hartmann, *Annu. Rev. Mater. Sci.* **29**, 53 (1999).

47. M. J. Freiser, *IEEE Trans. Magn.* **4(2)** 152 (1968).

48. Imada, S. Suga, W. Kuch, and J. Kirschner, *Surf. Rev. Lett.* **9(2)**, 877 (2002).

49. S. Valencia, A. Gaupp, W. Gudat, H.-Ch. Mertins, P. M. Oppeneer, D. Abramsohn, and C. M. Schneider, *New Journal of Physics*, **8**, 254 (2006).

50. P. Fischer, *IEEE J. Quantum Electron.*, **42(1)**, 36 (2006).

51. B.-S. Kang, D.-H. Kim, E. Anderson, P. Fischer, and G. Cho, *J. Appl. Phys*. **98**, 093907 (2005).

52. H. Stoll, A. Puzic, B. Van Waeyenberge, P. Fischer, J. Raabe, M. Buess, T. Haug, R. Hollinger, C. Back, D. Weiss, G. Denbeaux, *Appl. Phys. Lett.* **84**, 3328 (2004).

53. B. L. Mesler, P. Fischer, W. Chao, E. H. Anderson, and D.-H. Kim, *J. Vac. Sci. Technol. B* **25**, 2598 (2007).

54. M. Ohring, Materials Science of Thin Films: Deposition and Structure, (Academic Press, San Diego, 2002).

55. E. Gullikson. “Filter Transmission.” X-ray Interactions with Matter. http://henke.lbl.gov/optical_constants/ (July, 2010).

56. M. J. Madou, Fundamentals of Microfabrication: The Science of Miniaturization, 2nd ed. (CRC Press, Boca Raton, 2002).

57. K. Y. Guslienko, B. A. Ivanov, V. Novosad, Y. Otani, H. Shima, and K. Fukamichi, *J. Appl. Phys.* **91**, 8037 (2002).

58. S. Kasai, Y. Nakatani, K. Kobayashi, H. Kohno, and T. Ono, *Phys. Rev. Lett.* 97,107204 (2006).

59. K.-S. Lee and S.-K. Kim, *Phys. Rev. B* **78**, 014405 (2008).

60. K. Y. Guslienko, X. F. Han, D. J. Keavney, R. Divan, and S. D. Bader, *Phys. Rev. Lett.* **96**, 067205 (2006).

61. Y. Liu, S. Gliga, R. Hertel, and C. M. Schneider, *Appl. Phys. Lett.* **91**, 112501 (2007).

62. K. S. Buchanan, M. Grimsditch, F. Y. Fradin, S. D. Bader, and V. Novosad, *Phys. Rev. Lett.* **99**,267201 (2007).

63. B. L. Mesler, K. Buchanan, M.-Y. Im, and P. Fischer (in preparation).

64. A. A. Thiele, *Phys. Rev. Lett.* **30**, 230 (1973).

65. K. S. Buchanan, P. E. Roy, M. Grimsditch, F. Y. Fradin, K. Yu. Guslienko, S. D. Bader, and V. Novosad *Phys. Rev. B* **74**, 064404 (2006).

66. K.-S. Lee and S.-K. Kim, *Appl. Phys. Lett.* **91**, 132511 (2007).

67. K. Buchanan (in preparation)

68. K.-S. Lee, S.-K. Kim, Y.-S. Yu, Y.-S. Choi, K. Y. Guslienko, H. Jung, and P. Fischer, *Phys. Rev. Lett.* **101**, 267206 (2008).

69. A. Vansteenkiste, K. W. Chou, M. Weigand, M. Curcic, V. Sackmann, H. Stoll, T. Tyliszczak, G. Woltersdorf, C. H. Back, G. Shütz, and B. Van Waeyenberge, *Nat. Phys.* **5**, 332 (2009).

70. A. Bisig, J. Rhensius, M. Kammerer, M. Curcic, H. Stoll, G. Schütz, B. Van Waeyenberge, K. W. Chou, T. Tylisczak, L. J. Heyderman, S. Krzyk, A. von Bieren, and M. Kläui, *Appl. Phys. Lett.* **96**, 152506 (2010).

71. K.-S. Lee, private communication (2010).

72. W. Chao, B.H. Harteneck, J.A. Liddle, E.H. Anderson and D.T. Attwood, *Nature* **435**, 1210 (2005).

73. D.-H. Kim, P. Fischer, W. Chao, E. Anderson, M.-Y. Im, S.-C. Shin, and S.-B. Choe, *J. Appl. Phys.* **99**, 08H303 (2006).

74. W. Chao, J. Kim, S. Rekawa, P. Fischer, and E. H. Anderson, *Opt. Express* **17**, 17669 (2009).

75. P. Emma, R. Akre, J. Arthur, R. Bionta, C. Bostedt, J. Bozek, A. Brachmann, P. Bucksbaum, R. Coffee, F.-J. Decker, Y. Ding, D. Dowell, S. Edstrom, A. Fisher, J. Frisch, S. Gilevich, J. Hastings, G. Hays, Ph. Hering, Z. Huang, R. Iverson, H. Loos, M. Messerschmidt, A. Miahnahri, S. Moeller, H.-D. Nuhn, G. Pile, D. Ratner, J. Rzepiela, D. Schultz, T. Smith, P. Stefan, H. Tompkins, J. Turner, J.Welch, W. White, J. Wu, G. Yocky, and J. Galayda, *Nature Photon.* advance online publication, 1 August 2010 (DOI: 10.1038/nphoton.2010.176).

76. J. P. Park, P. Eames, D. M. Engebretson, J. Berezovsky, and P. A. Crowell, *Phys. Rev. B* **67**,020403(R) (2003).

77. J. Miltat and A. Thiaville, *Science* **298**, 555 (2002).

78. X. F. Han, M. Grimsditch, J. Meersschaut, A. Hoffmann, Y. Ji, J. Sort, J. Nogués, R. Divan, J. E. Pearson, and D. J. Keavney, *Phys. Rev. Lett.* **98**, 147202 (2007).

79. L. Bocklage, B. Krüger, R. Eiselt, M. Bolte, P. Fischer, and G. Meier, *Phys. Rev. B* **78**, 180405(R) (2008).

80. K. Kuepper, M. Buess, J. Raabe, C. Quitmann, and J. Fassbender, *Phys. Rev. Lett.* **99**, 167202 (2007).

81. D.-H. Kim, J.-H. Shim, B. L. Mesler, E. Anderson, P. Fisher, J.-H. Moon, and K.-J. Leeb (in preparation).

82. F. Alouges, T. Rivière, and S. Serfaty, *ESAIM Control Optim. Calc. Var.* **8**, 31 (2002).

83. R. Hertel, S. Gliga, M. Fähnle, and C. M. Schneider, *Phys. Rev. Lett.* **98**, 117201 (2007).

84. K.-S. Lee, K. Y. Guslienko, J.-Y. Lee, and S.-K. Kim, *Phys. Rev. B* **76**, 174410 (2007).

85. S. Choi, K.-S. Lee, K. Y. Guslienko, and S.-K. Kim, *Phys. Rev. Lett.* **98**,087205 (2007).

86. D. D. Sheka, Y. Gaididei, F. G. Mertens, *Appl. Phys. Lett.* **91**, 082509 (2007).

87. M. Buess, R. Hollinger, T. Haug, K. Perzlmaier, U. Krey, D. Pescia, M. R. Scheinfein, D. Weiss, and C. H. Back, *Phys. Rev. Lett.* **93**, 007207 (2004).

88. K.-J. Lee, A. Deac, O. Redon, J.-P. Nozieres, and B. Dieny, *Nature Mat.* **3**, 877 (2004).

89. J.-H. Moon, D.-H. Kim, M. H. Jung, and K.-J. Lee, *Phys. Rev. B* **79**, 134410 (2009).